ESD-TR-88-165

Technical Report
809

Tracking Targets with Bearing Data from a Single Sensor

W.H. Gilson

13 January 1989

Lincoln Laboratory
MASSACHUSETTS INSTITUTE OF TECHNOLOGY
LEXINGTON, MASSACHUSETTS

**Prepared for the Department of the Navy
under Electronic Systems Division Contract F19628-85-C-0002.**

ESD-TR-88-165

Technical Report
809

Tracking Targets with Bearing Data from a Single Sensor

W.H. Gilson

13 January 1989

Lincoln Laboratory

MASSACHUSETTS INSTITUTE OF TECHNOLOGY

LEXINGTON, MASSACHUSETTS

**Prepared for the Department of the Navy
under Electronic Systems Division Contract F19628-85-C-0002.**

The work reported in this document was performed at Lincoln Laboratory, a center for research operated by Massachusetts Institute of Technology. This work was sponsored by the Department of the Navy under Air Force Contract F19628-85-C-0002.

The ESD Public Affairs Office has reviewed this report, and it is releasable to the National Technical Information Service, where it will be available to the general public, including foreign nationals.

This technical report has been reviewed and is approved for publication.

FOR THE COMMANDER

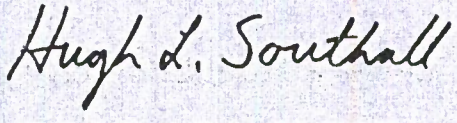

Hugh L. Southall, Lt. Col., USAF
Chief, ESD Lincoln Laboratory Project Office

Non-Lincoln Recipients

PLEASE DO NOT RETURN

Permission is given to destroy this document when it is no longer needed.

MASSACHUSETTS INSTITUTE OF TECHNOLOGY
LINCOLN LABORATORY

TRACKING TARGETS WITH BEARING DATA FROM A SINGLE SENSOR

W.H. GILSON
Group 36

TECHNICAL REPORT 809

13 JANUARY 1989

LEXINGTON MASSACHUSETTS

ABSTRACT

This report examines performance limits (Cramér-Rao bounds) on tracking a maneuvering target using bearing measurements from a single sensor on a maneuvering platform. An approximation to the Cramér-Rao bound for estimating the location, velocity, and acceleration of a constant acceleration target with a prior distribution of the target's velocity and acceleration is derived for the case where the target and the sensor are coplanar. The bound is computed for members of a two-parameter family of sensor trajectories, and optimal sensor trajectories within this two-parameter family are identified from contour plots of the bound vs the two parameters. The optimal trajectory in most cases is a weave around the line of sight to the target, with a period which is proportional to the observation time allotted for the measurement. The bound on performance is not in general very sensitive to either the sensor's or the target's motion, or to mismatch between the two, except that the period of the sensor's weave pattern influences both the time at which good estimates become available and the variance of the estimates after a given time interval.

The bounds indicate that passive ranging techniques should achieve rms range accuracies on the order of 10 to 20 percent, after 40 s of maneuvering, when the target bearing is measured with a 0.30° standard deviation bearing at a 1-s update rate. Range rate accuracies are expected to be relatively poor. Simulations of an iterative least-squares maximum *a posteriori* probability (MAP) estimator showed that the estimator performs at the level given by the bound and that it generates consistent estimates of the track accuracies. The estimator proved to be sensitive to target maneuvers that were not modeled within the estimation algorithm.

TABLE OF CONTENTS

Abstract iii
List of Illustrations vii
List of Tables xi

1. INTRODUCTION TO THE PROBLEM 1

2. THE CRAMÉR-RAO BOUND FOR BEARINGS-ONLY TRACKING 3

2.1. Formulation of the Estimation Problem 3
2.2. Cramér-Rao Bound and *A Priori* Information 5
2.3. Simplifications in a Coplanar Geometry 7

3. OPTIMAL TRAJECTORIES FOR BEARINGS-ONLY TRACKING 9

3.1. Sensor Maneuver Parameterization 9
3.2. Optimal Sensor Trajectories 11

4. ERROR BOUNDS FOR SUBOPTIMAL SENSOR TRAJECTORIES 25

5. MAXIMUM *A POSTERIORI* PROBABILITY TARGET TRACKS 41

6. CONCLUSIONS 49

APPENDIX — Iterative Least-Squares Estimator Equations 51

Acknowledgment 53

References 53

LIST OF ILLUSTRATIONS

Figure No.		Page
1	Plot of Sensor Trajectories for a Sensor Speed of 0.3 km/s and for Varying Maneuver Periods and Speeds. Each Curve Represents an x-y Plot of the Trajectory of a Sensor Platform with a Maneuver Period and a Speed Corresponding to the Starting Point Shown. The Curves Are Computed by Integrating Equations (3.1).	10
2	These Figures Show Two Target and Sensor Geometries for Which Exhaustive Searches for Optimal Sensor Maneuvers Were Carried Out. The Inbound Target in (a) Starts at 88 km on the y-Axis, and Travels at 0.3 km/s to 76 km, While the Crossing Target in (b) Starts at 70 km in y, –6 km in x and Travels to a Positive Displacement of 6 km in x. The Sensor Trajectory in Both Cases Has a 30 s Maneuver Cycle Time with a Speed and Maneuver Speed of 0.3 km/s. The Total Time in all Trajectories Shown Is 40 s.	13
3	The Position Bound Contour Plot Is Shown Here for the Case Analyzed by Olsder[20] and by Willman[21] of a Target with No Radial Velocity or Acceleration and with a Constant But Unknown Cross-Range Velocity. Local Minima Are Indicated by Cross-Hatched Boxes. This Plot Has a Global Minimum of 2.5 km at a Sensor Maneuver Speed of 0.3 km/s and a Maneuver Period of –44 s, with the Resulting Trajectory Shown in Figure 11(a).	14
4	The Velocity Bounds Are Shown for the Same Situation as in Figure 3. Local Minima Are Indicated by Cross-Hatched Boxes. The Global Minimum of 0.005 km/s Occurs at a Maneuver Speed of 0.18 km/s and at a Cycle Time of 76 s, at the Extreme of the Range Considered. The Resulting Trajectory Is Shown in Figure 11(b).	15
5	For the Contour Plot Given Here it Is Assumed to be Known *A Priori* that the Target Is Radially Inbound with a Lateral Acceleration Standard Deviation of 0.1 g and with a Velocity Standard Deviation of 0.05 km/s. The Other Parameters Are as Given in Table I. Local Minima Are Indicated by Cross-Hatched Boxes. The Global Minimum Is a Standard Deviation of 3.6 km at a Sensor Maneuver Velocity of 0.3 km/s and a Maneuver Period of 44 s, as Shown in Figure 11(c).	16

Figure No.		Page
6	This Plot of the Velocity Bounds Corresponds to the Position Bounds of Figure 5. Local Minima Are Indicated by Cross-Hatched Boxes. The Global Minimum Occurs at a Sensor Maneuver Velocity of 0.07 km/s and a Maneuver Period of -50 s, Resulting in the Trajectory Shown in Figure 11(d). The Value of the Minimum Standard Deviation, 0.048 km/s, Is Almost Equal to the *A Priori* Standard Deviation, Hence the Measurements Provide Little New Information.	17
7	Contour Plot of the Cramér-Rao Bound on the Position of the Target, with a Prior Velocity Standard Deviation of 0.4 km/s, and a Prior Acceleration Standard Deviation of 4 g. Local Minima Are Indicated by Cross-Hatched Boxes. The Global Minimum Is a Standard Deviation of 7.3 km at a Sensor Maneuver Velocity of 0.3 km/s and a Maneuver Period of 29 s; the Trajectory Is Shown in Figure 11(e).	18
8	This Figure Shows the Cramér-Rao Bounds for the Target Velocities for the Same Parameters as in Figure 7. Local Minima Are Indicated by Cross-Hatched Boxes. The Global Minimum Is a Standard Deviation of 0.32 km/s at a Sensor Maneuver Velocity of 0.14 km/s and a Maneuver Period of 42 s. The Trajectory for These Parameters Is Shown in Figure 11(f). Since the Minimum Velocity Standard Deviation, 0.32 km/s, Is Barely Smaller than the *A Priori* Standard Deviation of 0.4 km/s, One Can Conclude That the Measurements Provide Little Indication of the Target's True Radial Velocity.	19
9	The Position Bound Is Shown for an *A Priori* Velocity Standard Deviation of 100 km/s and an Acceleration Standard Deviation of 100 g, Which Represents Virtually No *A Priori* Information on the Target. Local Minima Are Indicated by Cross-Hatched Boxes. The Minimum of 9.8 km Occurs at a Maneuver Speed of 0.19 km/s and a Period of 54 s, and the Corresponding Trajectory Is Shown in Figure 11(g).	20
10	The Velocity Bound Is Shown Here for an *A Priori* Velocity Standard Deviation of 100 km/s and an Acceleration Standard Deviation of 100 g. Lcoal Minima Are Indicated by Cross-Hatched Boxes. The Minimum of 0.56 km/s Occurs at a Maneuver Speed of 0.14 km/s and a Period of 42 s. The Resulting Sensor Trajectory Appears in Figure 11(h).	21
11	Optimal Sensor Maneuvers for Various Degrees of *A Priori* Knowledge, as Listed in Table II. The Plots Are Grouped into Pairs, Wherein the Left Member Shows the Optimal Maneuver for Target Position Estimation and the Right Member Shows the Optimal Maneuver for Target Velocity Estimation.	22

Figure No.		Page
12	Ilustration of Target Trajectories Used in Bound Calculations, with Parameters as Shown in Table IV. The Symbol Marks the Position of the Target at the End of the Observation Time and Is Keyed to the Subsequent Plots in this Report. The Sensor Speed Is 0.3 km/s with a Maneuver Velocity of 0.3 km/s and a Cycle Time of 30 s. The Total Time Shown Here Is 120 s, and all Distances Are in Kilometers.	26
13	Cramér-Rao Bound vs Tracking Time for Case 1, Table V	29
14	Cramér-Rao Bound vs Tracking Time for Case 2, Table V	30
15	Cramér-Rao Bound vs Tracking Time for Case 3, Table V	31
16	Cramér-Rao Bound vs Tracking Time for Case 4, Table V	32
17	Cramér-Rao Bound vs Tracking Time for Case 5, Table V	33
18	Cramér-Rao Bound vs Tracking Time for Case 6, Table V	34
19	Cramér-Rao Bound vs Tracking Time for Case 7, Table V	35
20	Cramér-Rao Bound vs Tracking Time for Case 8, Table V	36
21	Cramér-Rao Bound vs Tracking Time for Case 9, Table V	37
22	Cramér-Rao Bound vs Tracking Time for Case 10, Table V	38
23	Cramér-Rao Bound vs Tracking Time for Case 11, Table V	39
24	Monte-Carlo Bias (Dashed) and rms Error (Dotted) for a Straight-Line Trajectory and Target Model	42
25	Plan View of a Single Run with a Straight-Line Target Trajectory and Model	43
26	Monte-Carlo Bias (Dashed) and rms Error (Dotted) with Cramér-Rao Bound (Solid) for a Straight-Line Target Trajectory But a Parabolic Trajectory Model	43
27	Plan View of a Single Run with a Straight-Line Target Trajectory But a Parabolic Model	44
28	Monte-Carlo Bias (Dashed) and rms Error (Dotted) with Cramér-Rao Bound (Solid) for a Parabolic Target Trajectory But a Straight-Line Target Trajectory Model	44
29	Plan Plot of a Single Run with a Parabolic Target Trajectory But a Straight-Line Target Model	45
30	Monte-Carlo Bias (Dashed) and rms Error (Dotted) with Cramér-Rao Bound (Solid) for a Parabolic Target Trajectory and Trajectory Model	45

Figure No.		Page
31	Plan View of a Sample Run with Parabolic Target Trajectory and Model Trajectory	46
32	Monte-Carlo Bias (Dashed) and rms Error (Dotted) for a Circular Target Path But a Parabolic Target Model	46
33	Plan View of a Single Run with a Circular Target Path But a Parabolic Target Model	47

LIST OF TABLES

Table No.		Page
I	Parameters for Exhaustive Search for Optimal Sensor Maneuvers	11
II	Parameters for Contour Plots of Position and Velocity Cramér-Rao Bounds	12
III	Optimization Results for Various Target Geometries, State Vector Components, and Observation Times, for the Parameters Given in Table I	24
IV	Parameters Describing the Motions of Targets at 70-km Range	25
V	Parameters for Figures 13 Through 21	28
VI	Key to Figures 24 Through 33	42

TRACKING TARGETS WITH BEARING DATA FROM A SINGLE SENSOR

1. INTRODUCTION TO THE PROBLEM

It is well established[1] that when bearings from only a single observer are available, the observer must maneuver in such a way that a component of the observer's acceleration is orthogonal to the line of sight to the target, in order to generate data from which the location and velocity of a target moving in a straight line can be estimated. It has also been shown that an extended Kalman filter for target position and velocity implemented in Cartesian coordinates experiences premature covariance collapse and divergence in bearings-only tracking applications.[2] On the other hand, several variations of the extended Kalman filter,[2,3] an iterative least-squares method,[4] and an approximate direct least-squares method[5] have been shown to achieve better performance. These are only a few of the many algorithms for bearings-only target tracking, or target motion analysis, that have been proposed.[6-19] Although there has been considerable research on this topic, important questions do not appear to have yet been properly addressed. In particular, there seem to be no published results on bounds or on estimates of the performance of bearings-only target tracking applied to maneuvering targets where there is some prior knowledge of likely velocities and accelerations. This report is an attempt to fill in the apparent gap in performance calculations for bearings-only tracking of maneuvering targets.

The work reported here concerns the accuracy with which one can estimate the location of a target using only bearing measurements taken from a moving sensor. By computing the Cramér-Rao lower bound on the variance of an unbiased estimator, one can study the properties of the measurement scenario, including *a priori* information, separately from the performance of particular estimators. Since it was found in this work that a maximum *a posteriori* probability (MAP) estimator performs at the level given by the bound, the bounds provide a meaningful view of bearings-only target tracking for any given measurement geometry and any given model of the target's motion. Operational considerations related to passive ranging are discussed in a separate report.

The target trajectory was modeled for this study as a parabola, i.e., as a constant acceleration trajectory. For many targets this is a realistic trajectory model, especially for short observation times, and it also has the benefits of being simple and of leading to a likelihood function that appears in simulations to have only one maximum. The *a priori* distributions of the target's velocity and acceleration are modeled as zero-mean Gaussian. The bounds calculated in this report are approximations to the Cramér-Rao bounds for estimating random variables with *a priori* distributions. The exact Cramér-Rao bound for estimating a random variable would be obtained from the expression for the Fisher information matrix computed as though the unknown were a nonrandom parameter, by averaging that expression over the *a priori* distribution of the random variable and adding the Fisher information matrix corresponding to the *a priori* distribution alone. In this work, the Fisher information matrices were not averaged over

the random variables, since they were not found in most cases to be very sensitive to the actual values of the target's velocity and acceleration over the range of likely *a priori* values. The bounds reported here are therefore approximations whenever the *a priori* information is significant. It was found to be unnecessary to include the height of the target in the vector of unknown quantities for the bound calculations, if the target and sensor remain coplanar throughout the observation time.

The influence of the sensor maneuvers was explored by making contour plots of the bounds for a family of sensor maneuvers parameterized by the magnitude of the changes in the component of the sensor platform's velocity orthogonal to the line of sight to the target and by the cycle time of the maneuvers. From these plots, optimal maneuvers within the two-parameter family of maneuvers can be found. The maneuvers thus obtained are optimal only within the family of maneuvers considered. Optimization of the sensor trajectory by means of optimal control theory[20] has been considered for a non-maneuvering target, and the results agree well with the two-parameter optimum obtained here. There has been other work on the performance limits for tracking maneuvering targets,[21] but the only target maneuvers considered were those orthogonal to the line of sight. It was also found in this work that the optimal trajectory for target position estimation is in general different from the optimal trajectory for target velocity estimation. The bounds, however, turn out to be relatively insensitive to mismatches between the postulated target motion for which the sensor maneuver is optimal and the actual target motion, and also to whether the trajectory is optimized for position measurement or velocity measurement. These issues will be covered in more detail once the theory and the computational details have been laid out. The usefulness of these Cramér-Rao bound calculations as an indication of estimation performance was verified by Monte-Carlo simulations of an iterative least-squares maximum *a posteriori* probability (MAP) estimator, which reached the performance limits set by the Cramér-Rao bound.

2. CRAMÉR-RAO BOUND FOR BEARINGS-ONLY TRACKING

The Cramér-Rao bound is a lower bound on the variance of unbiased estimators of a non-random parameter or of a random variable, and as such represents the best precision that one could hope to obtain. The Cramér-Rao bound depends in general on the probability density function of the measurements (Reference 22, pp. 79-85) but, as described in Section 2.2, a simpler formulation is available for additive white Gaussian noise under a state space description of the target's motion. The necessary propagation equations for the target motion, and the measurement relations, are presented in Section 2.1. In Section 2.3 a simplification of the bound computations is described, in the course of which the elevation angle is dropped from the measurement vector and the height of the target is dropped from the target state; this simplification leads to the same bound as before, if the target and the sensor are coplanar. Because of the significant reduction in computation time, this simplification was adopted for all bound computations in this study.

2.1. FORMULATION OF THE ESTIMATION PROBLEM

The estimation problem is posed as follows. A target is moving along a parabolic path described by the 9-dimensional state vector

$$\mathbf{x}^t = \begin{bmatrix} x^t \\ \dot{x}^t \\ \ddot{x}^t \\ y^t \\ \dot{y}^t \\ \ddot{y}^t \\ z^t \\ \dot{z}^t \\ \ddot{z}^t \end{bmatrix} \tag{2.1}$$

The degenerate case of linear target motion arises when the second derivative entries are zero. The measurements of the target bearing are made from a sensor on a platform that is moving along an arbitrary trajectory given by $\mathbf{x}^s(t) = [x^s(t), y^s(t)]$. These measurements are taken at a fixed interval T_s and are corrupted by additive Gaussian noise that is independent and identically distributed from measurement to measurement. With the definition of $\mathbf{x}_n^t$ as the state of the target when sample n is taken, the target state propagates according to the equation

$$\mathbf{x}_{n+1}^t = \mathbf{F}\mathbf{x}_n^t \quad , \tag{2.2}$$

where the propagation matrix **F** is a block diagonal matrix with three identical 3×3 blocks,

$$\mathbf{F} = \begin{pmatrix} \mathbf{F}' & 0 & 0 \\ 0 & \mathbf{F}' & 0 \\ 0 & 0 & \mathbf{F} \end{pmatrix} , \tag{2.3}$$

each block of which is given by

$$\mathbf{F}' = \begin{pmatrix} 1 & T_s & \frac{1}{2} T_s^2 \\ 0 & 1 & T_s \\ 0 & 0 & 1 \end{pmatrix} . \tag{2.4}$$

Each measurement is a vector **r**, equal to a measurement function **h** composed of a bearing θ and an elevation ϕ,

$$\mathbf{h} \equiv \begin{pmatrix} \theta \\ \phi \end{pmatrix} \tag{2.5}$$

plus noises w_θ and w_ϕ:

$$\mathbf{r} = \begin{pmatrix} \theta \\ \phi \end{pmatrix} + \begin{pmatrix} w_\theta \\ w_\phi \end{pmatrix} . \tag{2.6}$$

The measured angles are given in terms of the target and sensor coordinates at the time of the measurements by

$$\theta = \tan^{-1} \frac{x^t - x^s}{y^t - y^s}$$

and

$$\theta = \tan^{-1} \frac{z^t - z^s}{[(x^t - x^s)^2 + (y^t - y^s)^2]^{1/2}} . \tag{2.7}$$

The linearized observation matrix, which will be necessary both for evaluating the bound and for implementing the MAP estimator, is defined in terms of the measurement function **h** as

$$\mathbf{H} = \nabla_{x^t} \mathbf{h}$$

$$= \begin{pmatrix} \nabla_{x^t} \theta \\ \nabla_{x^t} \phi \end{pmatrix} . \tag{2.8}$$

The nonzero derivatives are shown below:

$$\frac{\partial\theta}{\partial x^t} = \frac{\Delta y}{R_g^2}$$

$$\frac{\partial\theta}{\partial y^t} = -\frac{\Delta x}{R_g^2}$$

$$\frac{\partial\phi}{\partial x^t} = -\frac{\Delta x \Delta z}{R_g R^2} \tag{2.9}$$

$$\frac{\partial\phi}{\partial y^t} = -\frac{\Delta y \Delta z}{R_g R^2}$$

$$\frac{\partial\phi}{\partial z^t} = \frac{R_g}{R^2}$$

with these definitions:

$$\begin{aligned} \Delta x &= x^t - x^s \\ \Delta y &= y^t - y^s \\ \Delta z &= z^t - z^s \\ R_g &= \sqrt{\Delta x^2 + \Delta y^2} \\ R &= \sqrt{\Delta x^2 + \Delta y^2 + \Delta z^2} \end{aligned} \tag{2.10}$$

(R_g is the horizontal distance between the target and the sensor.) The noises w_θ and w_ϕ have the autocovariance matrix

$$\mathbf{R} = \sigma_a^2 \begin{pmatrix} 1 & 0 \\ 0 & 1 \end{pmatrix} . \tag{2.11}$$

The expressions given in Equation (2.7) for the angles and in Equation (2.10) for the angle noise may give slightly incorrect values depending on the physical implementation of the angle measurements and on the geometry. Such errors should be small except for when the target and sensor are at very different altitudes and at close ranges.

2.2 CRAMÉR-RAO BOUNDS AND *A PRIORI* INFORMATION

The Fisher information matrix for estimating the current target state $\mathbf{x}_N^t$ for a target with initial state $\mathbf{x}_0^t$, without *a priori* information, using measurements taken at time indices 1 through

N, is given[23] by the recursions

$$\mathbf{x}_n^t = \mathbf{F}\mathbf{x}_{n-1}^t$$

and

$$\mathbf{J}_n(\mathbf{x}_0^t) = (\mathbf{F}^{-1})^T\, \mathbf{J}_{n-1}(\mathbf{x}_0^t)\, \mathbf{F}^{-1} + \mathbf{H}_n^T\mathbf{R}^{-1}\mathbf{H}_n \quad . \tag{2.12}$$

The Cramér-Rao lower bound on the variance of say element μ of the state vector $\mathbf{x}_N^t$, is given (Reference 22, p. 79) by:

$$\mathrm{var}[\hat{\mathbf{x}}_N^t]_\mu \geq [\mathbf{J}_N^{-1}(\mathbf{x}_0^t)]_{\mu\mu} \quad . \tag{2.13}$$

The starting point of the recursion is

$$\mathbf{J}_0 = 0 \quad . \tag{2.14}$$

If on the other hand there is Gaussian *a priori* information, the target state is treated as a random variable (Reference 22, pp. 84-85). The Fisher information matrix $\mathbf{J}_N(\mathbf{x}_0^t)$, representing information available from the data, is computed as before, but the bound is obtained somewhat differently. First, the matrix $\mathbf{J}_n(\mathbf{x}_0^t)$ must be averaged over the prior density $p_0(\mathbf{x}_N^t)$ of the final target state and added to the *a priori* information matrix

$$\mathbf{J}^A = \{E[\hat{\mathbf{x}}_N^t(\hat{\mathbf{x}}_N^t)^T]\}^{-1} \quad , \tag{2.15}$$

to form the Bayesian information matrix

$$\mathbf{J}_N^B = \mathbf{J}^A + \int d\mathbf{x}_N^t\, \mathbf{J}_N(\mathbf{F}^{-N}\mathbf{x}_N^t)\, p_0(\mathbf{x}_N^t) \quad . \tag{2.16}$$

The bound is then given by

$$\mathrm{var}[\hat{\mathbf{x}}_N^t]_\mu \geq [(\mathbf{J}_N^B)^{-1}]_{\mu\mu} \quad . \tag{2.17}$$

This procedure produces a bound that is averaged over all possible target states and is therefore independent of the actual state. To the degree that the Fisher information matrix is insensitive to the actual target states within the *a priori* distribution of states, the averaged Fisher information matrix $\mathbf{J}_N^B$ is equal to the Fisher information matrix $\mathbf{J}_N(\mathbf{x}_0^t)$ evaluated at one given state. Even if the Fisher information matrix does depend on the target state, the approximate "bound" given by Equation (2.13) but with a nonzero *a priori* information matrix $\mathbf{J}_N^A$ added in provides an indication of how the integrand varies with the target state, and to the degree that $\mathbf{J}_N(\mathbf{x}_0^t)$ is insensitive to the initial target state $\mathbf{x}_0^t$, this "bound" is an approximation to the Cramér-Rao bound computed from the averaged Fisher information matrix $\mathbf{J}_N^B$. Since the approximate Cramér-Rao bounds calculated below (Figures 13 to 23) show overall relatively little dependence on the target state, the bound evaluated for a given target state is an adequate approximation to the bound computed from the expected value of the Fisher information matrix over the *a priori* distribution

of target states. Where the approximate bound does depend on the target state, it is an indicator of the sensitivity of passive ranging performance to the target state.

From these formulations one can make some general inferences about the behavior of the error bounds. In the absence of *a priori* information, the bound is proportional to the angle measurement variance. When the sampling interval T_s is sufficiently short compared with the time scales of the sensor and target maneuvers, the recursion result can be approximated by an integral, and the bound is then proportional to the sampling interval.

2.3 SIMPLIFICATIONS IN A COPLANAR GEOMETRY

When the trajectories of the sensor and the target lie in the same plane, the uncertainty in the altitude of the target can be dropped from the bound computation. This follows from the dependence of the derivatives of the elevation angle on the relative height of the target and the sensor and from the structure of the Fisher information matrix. Because the derivatives of the elevation with respect to the target x and y coordinates are zero when the difference between the sensor and the target elevations Δz is zero [Equation (2.9)], the linearized measurement matrix **H** takes the form

$$\mathbf{H} = \begin{pmatrix} \frac{\partial\theta}{\partial x^t} & 0 & 0 & \frac{\partial\theta}{\partial y^t} & 0 & 0 & 0 & 0 & 0 \\ 0 & 0 & 0 & 0 & 0 & 0 & \frac{\partial\phi}{\partial z^t} & 0 & 0 \end{pmatrix} , \tag{2.18}$$

and the incremental term in the recursion formula, Equation (2.12), for the Fisher information matrix, takes the form

$$\mathbf{H}^T\mathbf{R}^{-1}\mathbf{H} = \frac{1}{\sigma_a^2}\begin{bmatrix} \left(\frac{\partial\theta}{\partial x^t}\right)^2 & 0 & 0 & \frac{\partial\theta}{\partial x^t}\frac{\partial\theta}{\partial y^t} & 0 & 0 & 0 & 0 & 0 \\ 0 & 0 & 0 & 0 & 0 & 0 & 0 & 0 & 0 \\ 0 & 0 & 0 & 0 & 0 & 0 & 0 & 0 & 0 \\ \frac{\partial\theta}{\partial x^t}\frac{\partial\theta}{\partial y^t} & 0 & 0 & \left(\frac{\partial\theta}{\partial y^t}\right)^2 & 0 & 0 & 0 & 0 & 0 \\ 0 & 0 & 0 & 0 & 0 & 0 & 0 & 0 & 0 \\ 0 & 0 & 0 & 0 & 0 & 0 & 0 & 0 & 0 \\ 0 & 0 & 0 & 0 & 0 & 0 & \left(\frac{\partial\theta}{\partial z^t}\right)^2 & 0 & 0 \\ 0 & 0 & 0 & 0 & 0 & 0 & 0 & 0 & 0 \\ 0 & 0 & 0 & 0 & 0 & 0 & 0 & 0 & 0 \end{bmatrix} \tag{2.19}$$

In the recursion given by Equation (2.12) the 3×3 blocks of the incremental term, Equation (2.19), are multiplied by the block diagonal propagator $\mathbf{F}$ of Equation (2.4). This multiplication leaves the overall block structure of $\mathbf{H}^T\mathbf{H}$ unchanged, as it propagates values within the 3×3 blocks. Hence the 3×3 block of the Fisher information matrix that corresponds to elevation measurement, consisting of rows and columns 7 through 9, remains uncoupled from the remaining 3×3 blocks on the diagonal, corresponding to x and y position measurement. The reduction in rank from a 9×9 matrix to a 6×6 matrix leads to a sizable savings in the computation time for the bounds.

3. OPTIMAL TRAJECTORIES FOR BEARINGS-ONLY TRACKING

To determine the best performance that one could possibly achieve with bearings-only tracking, one must first identify the optimal maneuvers for the sensor. There has been at least one attempt to use optimal control methods to search for the optimal path that minimizes the Cramér-Rao bound on range estimation,[20] but the slope-following minimization procedure on which the optimal control method employed in Reference 20 relies can get trapped in false local minima and can consequently produce erroneous solutions. For the present work, an exhaustive search procedure was used instead. The usual difficulty with exhaustive searches is of course the amount of computation required, and here the computation is limited by constraining the search to a two-parameter family of trajectories. The decision to avoid a slope-following search was subsequently justified, as the bound did indeed display multiple minima for various sensor maneuvers (Figures 3 to 10).

An additional issue covered in this study is the distinction between trajectories optimized for range estimation and trajectories optimized for range rate estimation. For tracking, one needs not only the target's range but also its range rate, and so both the Cramér-Rao bound on the variance of the estimated range and the Cramér-Rao bound for the range rate should be considered separately as performance measures. As shown below, the two measures yield different optimal maneuvers.

3.1 SENSOR MANEUVER PARAMETERIZATION

It was decided initially to perform an exhaustive search for the optimal sensor trajectory over a finite sampling of a few parameters rather than to try a slope-following minimization algorithm. In order to keep the dimensionality of the search space small, the possible sensor trajectories were represented by a family of curves parameterized by only the sensor platform speed, the cycle time of its maneuvers, and the variation in the cross-range component of the sensor platform's velocity during maneuvering, as described in the next paragraph. All the maneuvers were described with reference to the direction of the line of sight to the target, so that a rotation of the initial bearing to the target results in a rotation of the sensor platform's maneuver. This keeps the relative trajectory of the sensor to the target independent of the initial bearing of the target.

The family of sensor trajectories for a target along the y-axis, when the sensor is at or near the origin, are generated by the following equations of motion:

$$\begin{aligned} \dot{x}^s &= v - \Delta v(1 + \sin 2\pi t/T_m) \\ \dot{y}^s &= \sqrt{v^2 - (\dot{x}^s)^2} \end{aligned} \tag{3.1}$$

where v is the sensor speed, presumed constant, T_m is the period of the sensor's maneuvers, and Δv is the speed that is "devoted" to maneuvering. The maneuver period can take on positive or negative values, and these two possibilities give rise to different trajectory shapes. A negative maneuver period causes in effect a phase shift of the weave pattern relative to the time at which the maneuver begins. Figure 1 shows an assortment of sensor trajectories for a distant target on

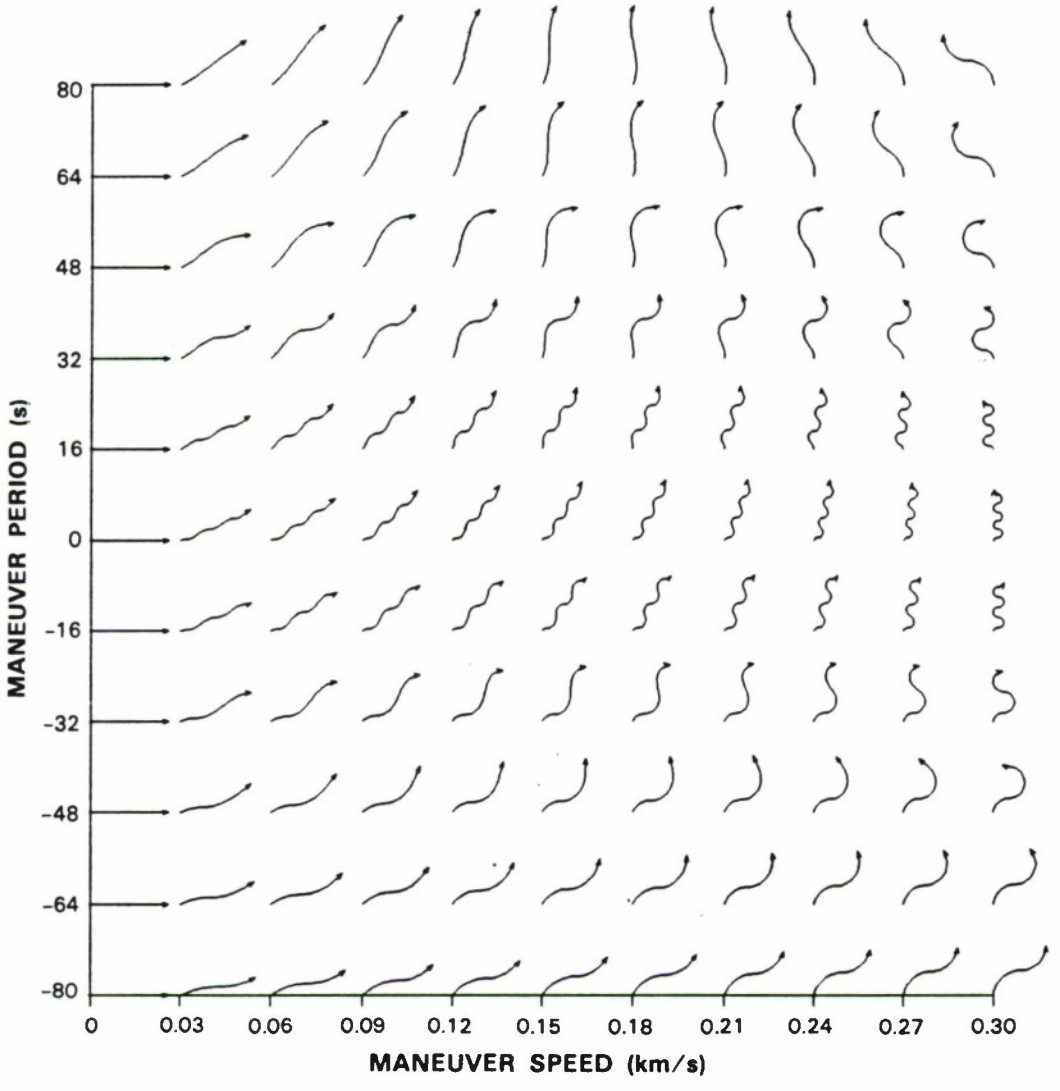

Figure 1. Plot of sensor trajectories for a sensor speed of 0.3 km/s and for varying maneuver periods and speeds. Each curve represents an x-y plot of the trajectory of a sensor platform with a maneuver period and a speed corresponding to the starting point shown. The curves are computed by integrating Equations (3.1).

the y-axis for a sensor platform moving at 0.3 km/s (Mach 0.87), with Δv varying between 0 and v, and for sensor maneuver periods varying between –60 and 60 s. The total time in the examples is 120 s. When the target and sensor are at arbitrary points in the x-y plane, these equations change. The x-component of the sensor velocity given in Equation (3.1) is rotated to lie orthogonal to the line of sight to the target and the y-component is rotated to lie along the line of sight. Thus

$$\begin{pmatrix} \dot{x}^s \\ \dot{y}^s \end{pmatrix} = \frac{1}{R_g} \begin{pmatrix} \Delta y & \Delta x \\ -\Delta x & \Delta y \end{pmatrix} \begin{bmatrix} v - \Delta v(1 + \sin 2\pi t/T_m) \\ \sqrt{v^2 - (\dot{x}^s)^2} \end{bmatrix} . \qquad (3.2)$$

3.2 OPTIMAL SENSOR TRAJECTORIES

An efficient means of presenting exhaustive search computations was found to be via contour plots of the range and range rate bounds. The parameters for the contour plots in Figures 3 to 10 are given in Tables I and II. The target trajectory for which these contour plots were obtained is shown in Figure 2(a), and the optimum trajectories found are shown in Figure 11, following the indications in Table II. The contour plots of the bound indicate the limit on the achievable performance as a function of the trajectory of the sensor platform, and they show how the optimal trajectory depends on whether it is optimized for position or for velocity and on the degree of *a priori* information on the target. The plots disclose the existence, suggested at the beginning of Section 3, of local minima for sensor maneuvers, which could indeed trap a slope-following minimization procedure. It might be feasible, however, to use local minima found using a parameterization such as that described here as starting points for a slope-following algorithm with many more degrees of freedom. As will be discussed below, the plots also suggest that the parameterization chosen does seem to yield performances approximating those obtained by a more general maneuver optimization procedure.

In the contour plots shown here, the horizontal axis is the sensor velocity used in maneuvering, and the vertical axis is the cycle time of the maneuver. As listed in Table I, the total sensor platform speed is fixed at 0.3 km/s and the total observation time is also fixed at 40 s. The value actually contoured is the approximate lower limit on the standard deviation given by the Cramér-Rao computed as described in Section 2, for either the range or the range rate of the target. For all contour plots, the target is inbound starting at 76 km from the origin along the y-axis and ending, after 40 s, at 64 km from the origin. The sensor always starts at the origin. The standard deviation of the bearing measurements is always 0.3°, with an update interval of 1 s. It is assumed that the prior distributions of the target's velocity and acceleration are independent zero-mean Gaussian distributions in each coordinate, x and y, with standard deviations listed in Table II.

TABLE I

Parameters for Exhaustive Search for Optimal Sensor Maneuvers

Bearing Standard Deviation (deg)	0.3
Sample Interval (s)	1
Sensor Platform Speed (km/s)	0.3
Sensor Starting Point (km)	(0, 0)
Observation Time (s)	40

TABLE II

Parameters for Contour Plots of Position and Velocity Cramér-Rao Bounds

Figure	*A Priori* σ_{vel} (km/s)	*A Priori* σ_{accel} (g)	Optimized for	Δv (km/s)	T_m (s)	Figure 11 Plot	Bound at Optimum
3	0.001 radial 100 crossing	0.01	position	0.3	44	(a)	2.5 km
4	0.001 radial 100 crossing	0.01	position	0.18	76	(b)	0.05 km/s
5	0.05	0.1	position	0.3	44	(c)	3.6 km
6	0.5	0.1	velocity	0.07	50	(d)	0.05 km/s
7	0.4	4	position	0.3	29	(e)	7.3 km
8	0.4	4	velocity	0.17	42	(f)	0.32 km/s
9	100	1000	position	0.19	54	(g)	9.8 km
10	100	1000	velocity	0.14	42	(h)	0.56 km/s

The fifth through seventh columns specify the optimal sensor maneuver and the eighth column gives the bound obtained with the optimal maneuver.

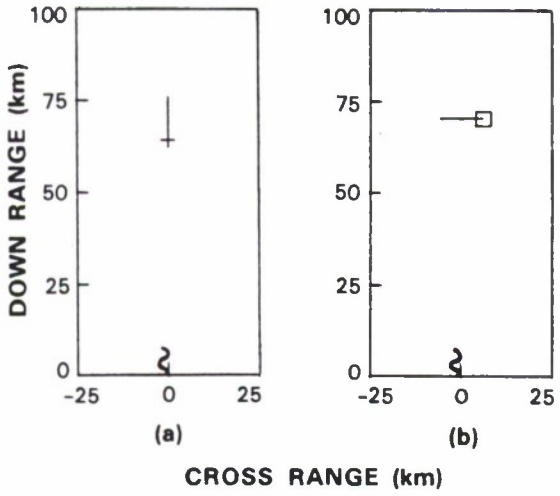

101776-2

Figure 2. These figures show two target and sensor geometries for which exhaustive searches for optimal sensor maneuvers were carried out. The inbound target in (a) starts at 88 km on the y-axis, and travels at 0.3 km/s to 76 km, while the crossing target in (b) starts at 70 km in y, –6 km in x, and travels to a positive displacement of 6 km in x. The sensor trajectory in both cases has a 30-s maneuver cycle time with a speed and maneuver speed of 0.3 km/s. The total time in all trajectories shown is 40 s.

A small quantity equivalent to an *a priori* position standard deviation of 1000 km is added to the diagonal elements of the Fisher information matrix that correspond to the target x and y positions in order to make the matrix non-singular. Once the information from the data exceeds that from the *a priori* distribution of the parameters, the effect of adding this quantity to the information is negligible.

The plots in Figures 3 and 4 were obtained in order to provide a comparison of the present maneuver parameterization with the optimal maneuver found in Reference 20, assuming a known (or negligible) target range rate and a known (or negligible) acceleration. These represent the conditions under which the maneuver was optimized in Reference 20, using a slope-following procedure with many degrees of freedom. For these same conditions, an approximate expression for the Cramér-Rao bound on the target range estimation standard deviation is given in Reference 21. The optimal trajectory for ranging a target with known range rate and known acceleration was found in Reference 20 to consist of two approximately straight line segments of the same length nearly orthogonal to the line of sight, and in Reference 21, it was shown that for such a trajectory the Cramér-Rao bound on the target range estimate for a distant target is given by

$$\frac{4\sigma_a R^2}{v}\sqrt{\frac{3T_s}{T_o^3}} \tag{3.3}$$

where T_o is the total observation time and R is the range of the target. The contour plots shown in Figure 3 display two nearly equivalent minima at sensor maneuver periods of ±40-s and a

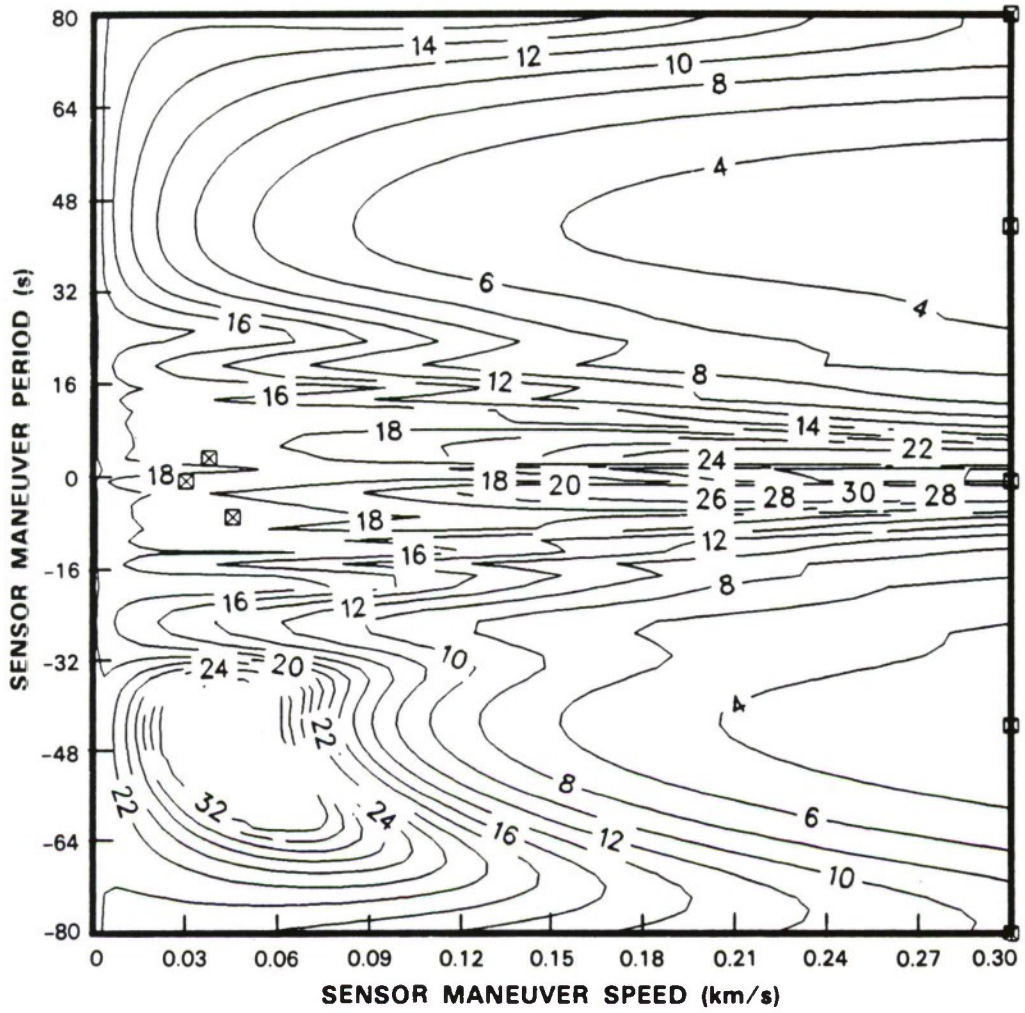

Figure 3. The position bound contour plot is shown here for the case analyzed by Olsder[20] and by Willman[21] of a target with no radial velocity or acceleration and with a constant but unknown cross-range velocity. Local minima are indicated by cross-hatched boxes. This plot has a global minimum of 2.5 km at a sensor maneuver speed of 0.3 km/s and a maneuver period of -44 s, with the resulting trajectory shown in Figure 11(a).

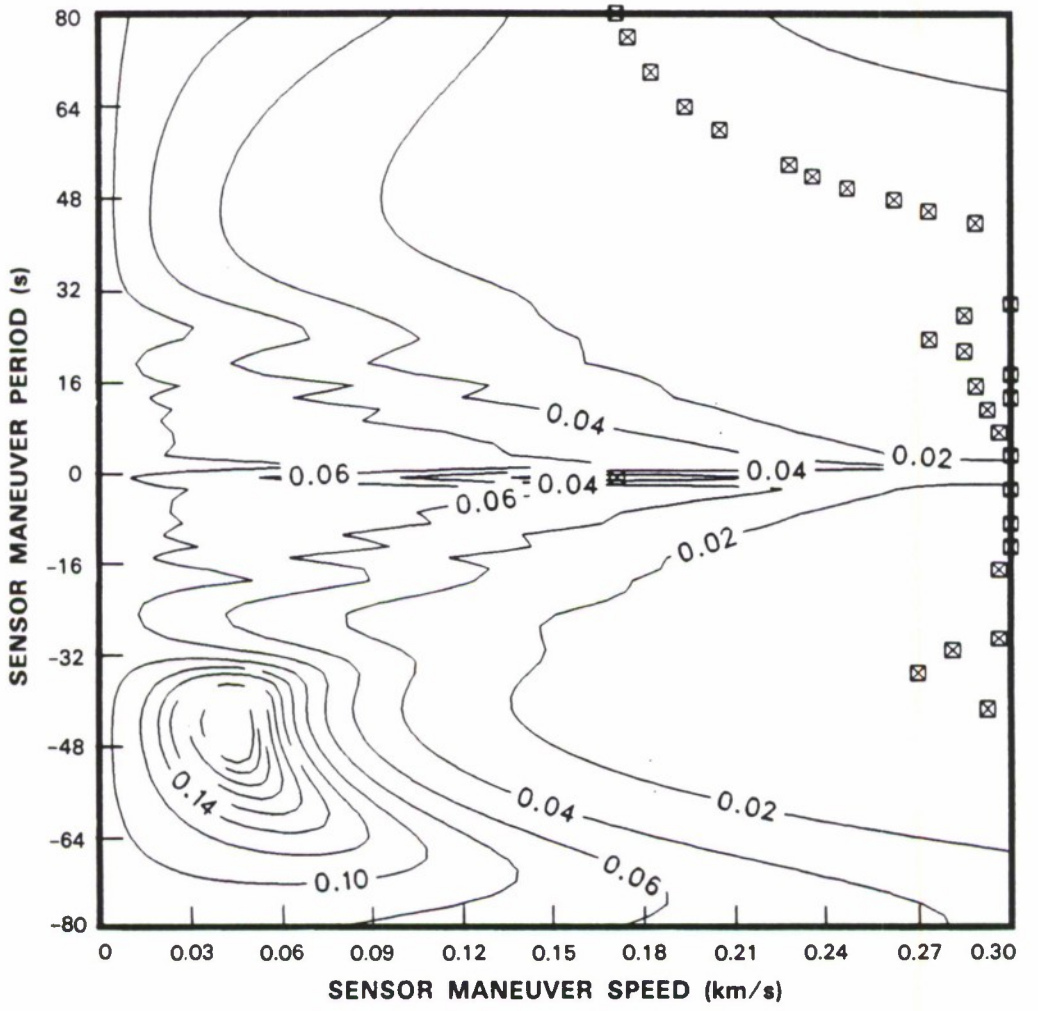

101776-4

Figure 4. The velocity bounds are shown for the same situation as in Figure 3. Local minima are indicated by cross-hatched boxes. The global minimum of 0.005 km/s occurs at a maneuver speed of 0.18 km/s and at a cycle time of 76 s, at the extreme of the range considered. The resulting trajectory is shown in Figure 11(b).

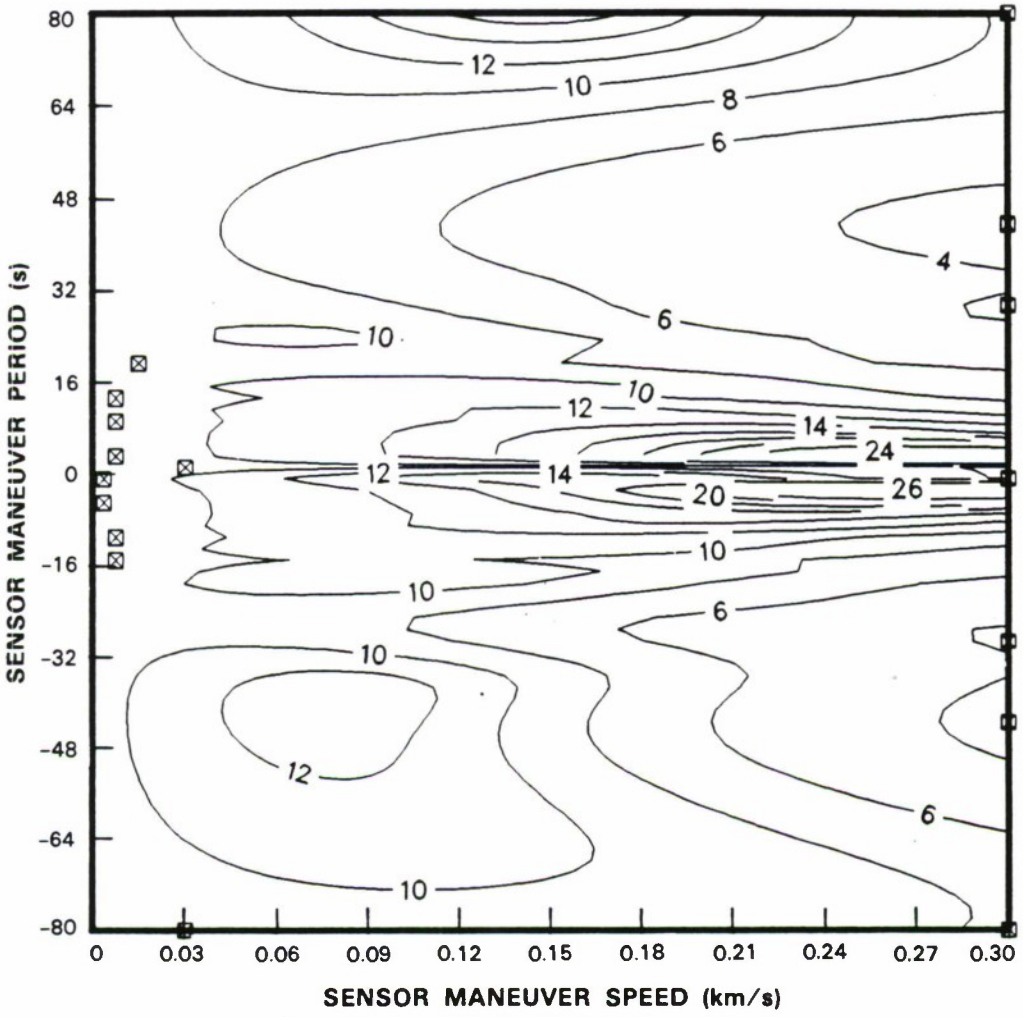

101776-5

Figure 5. For the contour plot given here it is assumed to be known a priori that the target is radially inbound with a lateral acceleration standard deviation of 0.1 g and with a velocity standard deviation of 0.05 km/s. The other parameters are as given in Table I. Local minima are indicated by cross-hatched boxes. The global minimum is a standard deviation of 3.6 km at a sensor maneuver velocity of 0.3 km/s and a maneuver period of 44 s, as shown in Figure 11(c).

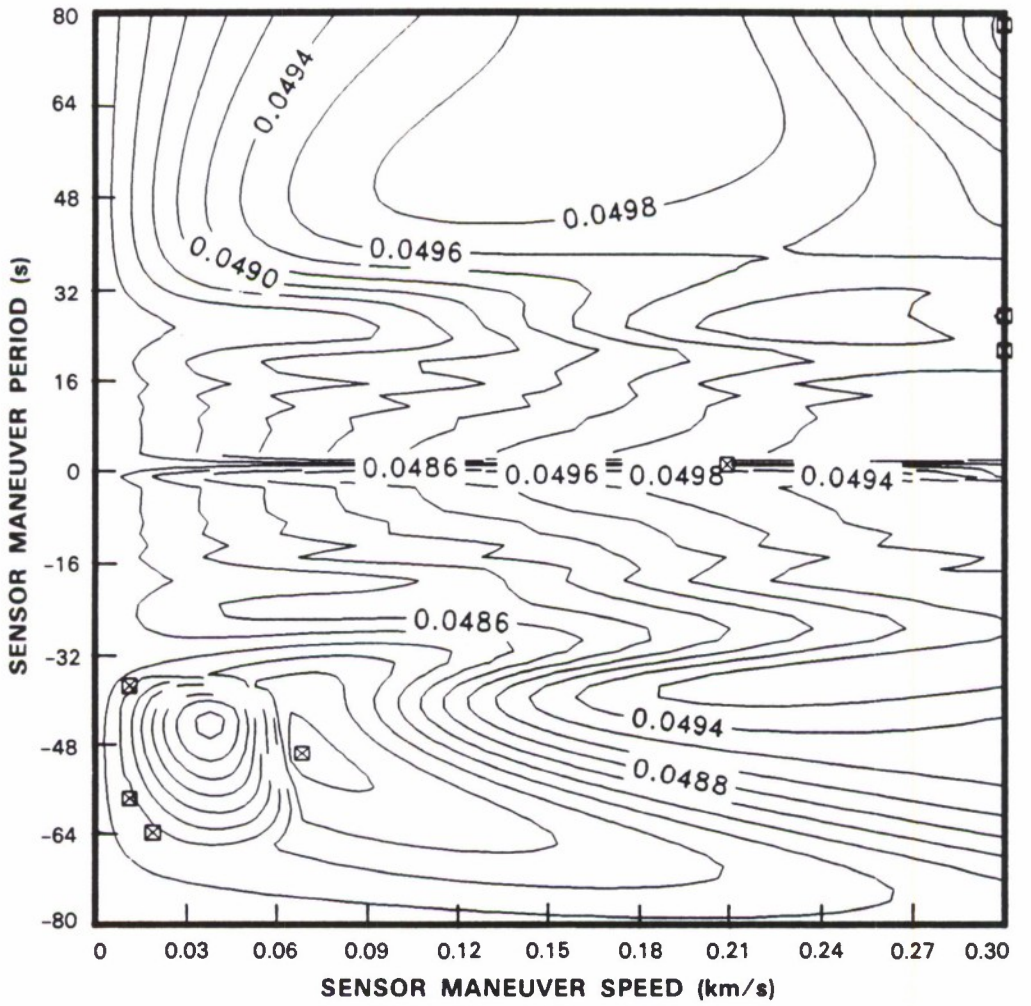

101776-6

Figure 6. This plot of the velocity bounds corresponds to the position bounds of Figure 5. Local minima are indicated by cross-hatched boxes. The global minimum occurs at a sensor maneuver velocity of 0.07 km/s and a maneuver period of -50 s, resulting in the trajectory shown in Figure 11(d). The value of the minimum standard deviation, 0.048 km/s, is almost equal to the a priori standard deviation, hence the measurements provide little new information.

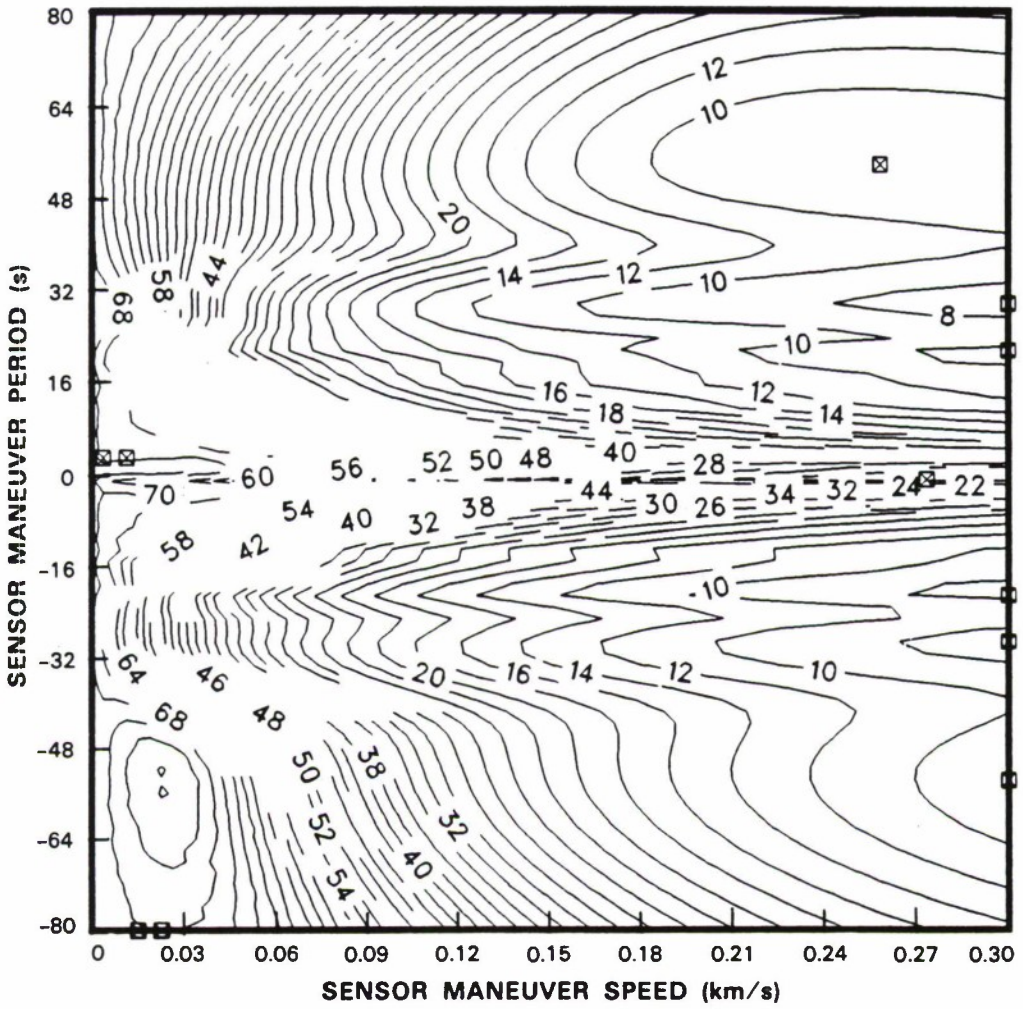

Figure 7. Contour plot of the Cramér-Rao bound on the position of the target, with a prior velocity standard deviation of 0.4 km/s, and a prior acceleration standard deviation of 4 g. Local minima are indicated by cross-hatched boxes. The global minimum is a standard deviation of 7.3 km at a sensor maneuver velocity of 0.3 km/s and a maneuver period of 29 s; the trajectory is shown in Figure 11(e).

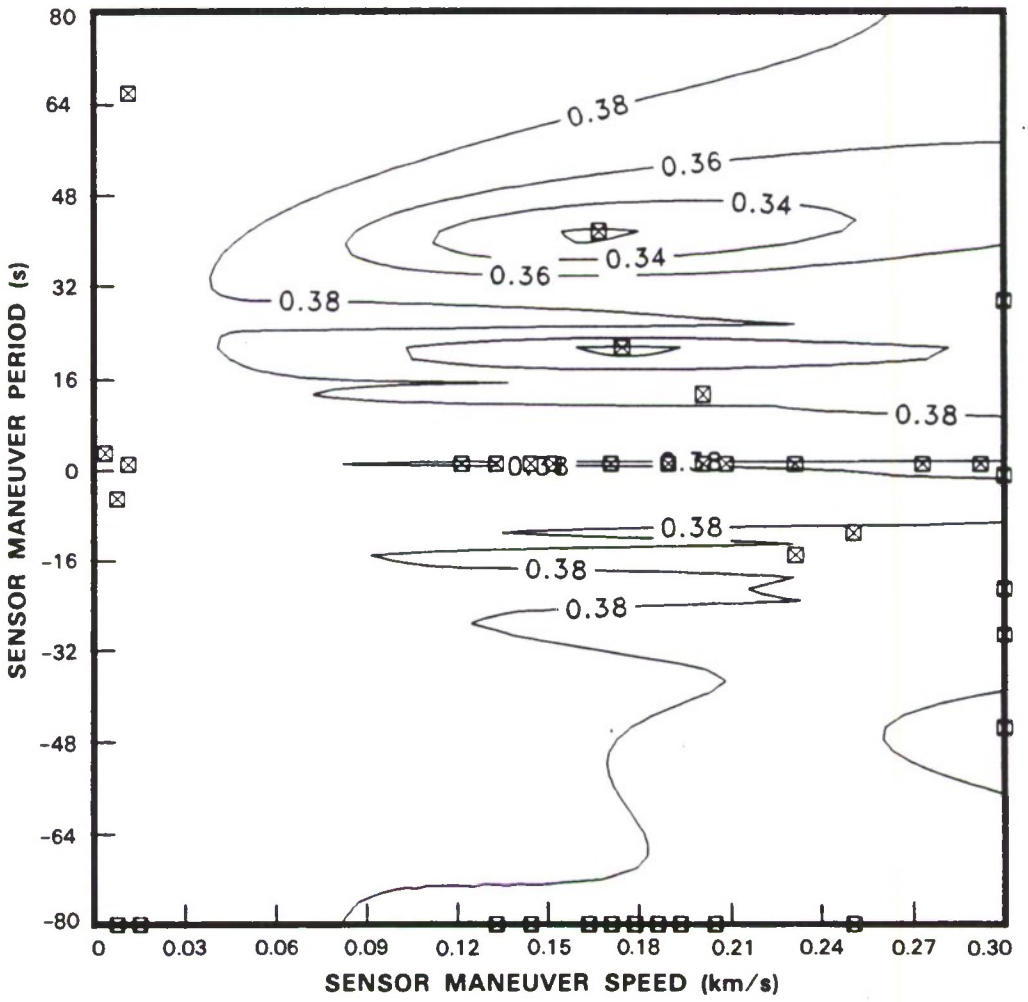

101776-8

Figure 8. This figure shows the Cramér-Rao bounds for the target velocities for the same parameters as in Figure 7. Local minima are indicated by cross-hatched boxes. The global minimum is a standard deviation of 0.32 km/s at a sensor maneuver velocity of 0.14 km/s and a maneuver period of 42 s. The trajectory for these parameters is shown in Figure 11(f). Since the minimum velocity standard deviation, 0.32 km/s, is barely smaller than the a priori standard deviation of 0.4 km/s, one can conclude that the measurements provide little indication of the target's true radial velocity.

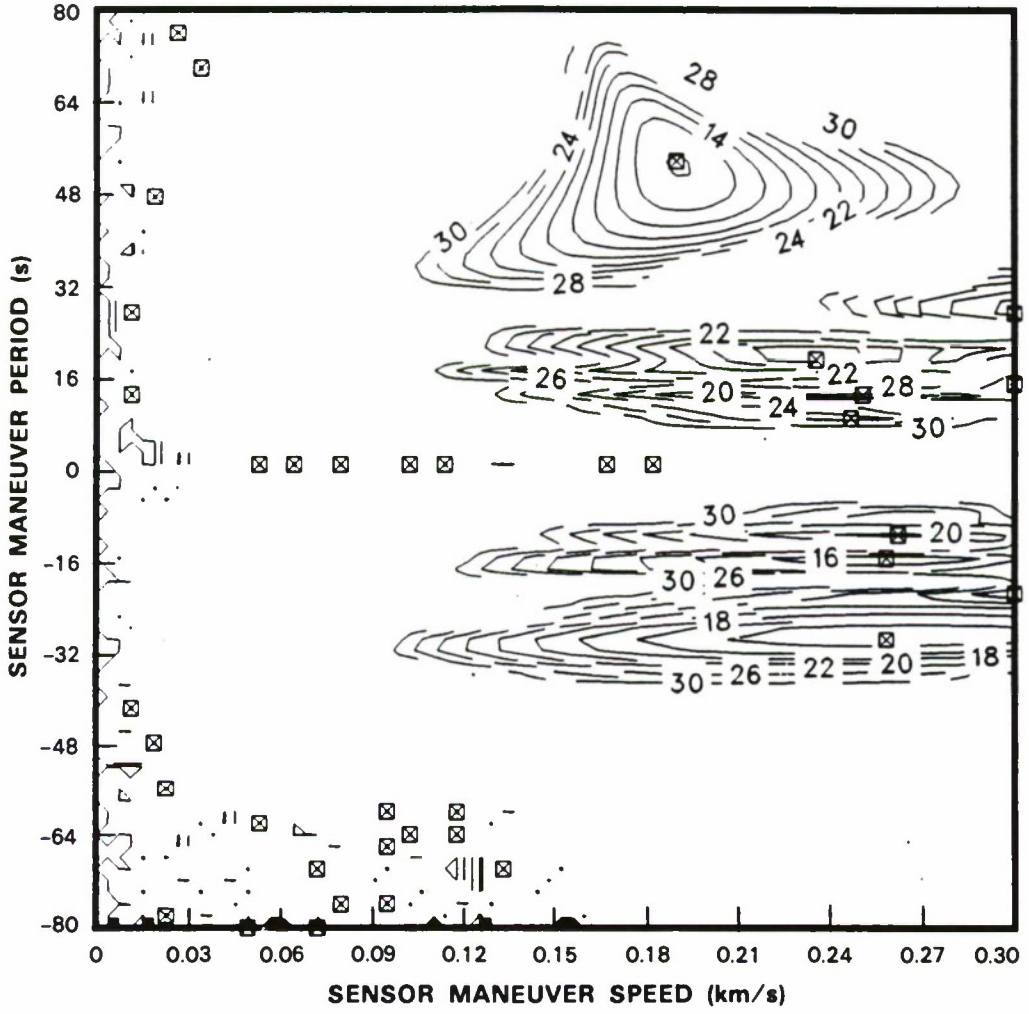

Figure 9. The position bound is shown for an a priori velocity standard deviation of 100 km/s and an acceleration standard deviation of 100 g, which represents virtually no a priori information on the target. Local minima are indicated by cross-hatched boxes. The minimum of 9.8 km occurs at a maneuver speed of 0.19 km/s and a period of 54 s, and the corresponding trajectory is shown in Figure 11(g).

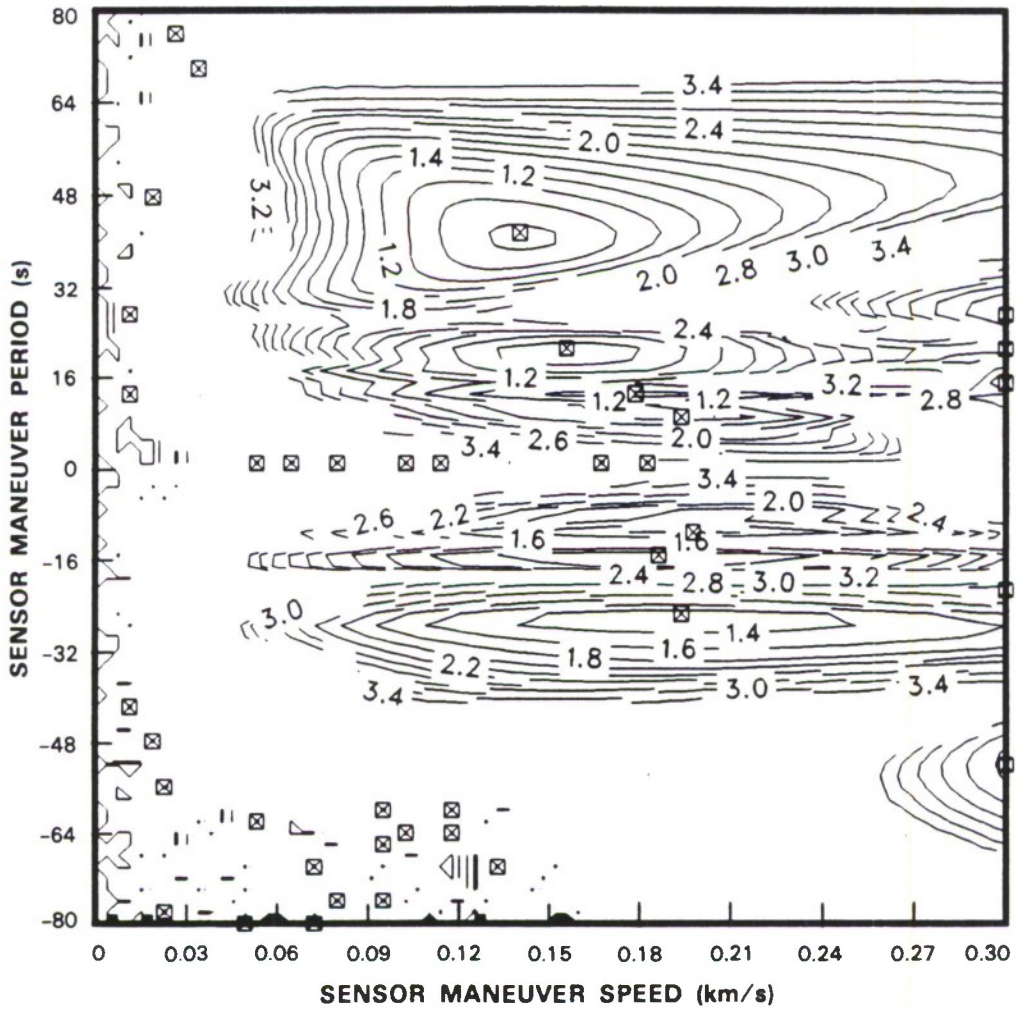

Figure 10. The velocity bound is shown here for an a priori velocity standard deviation of 100 km/s and an acceleration standard deviation of 100 g. Local minima are indicated by cross-hatched boxes. The minimum of 0.56 km/s occurs at a maneuver speed of 0.14 km/s and a period of 42 s. The resulting sensor trajectory appears in Figure 11(h).

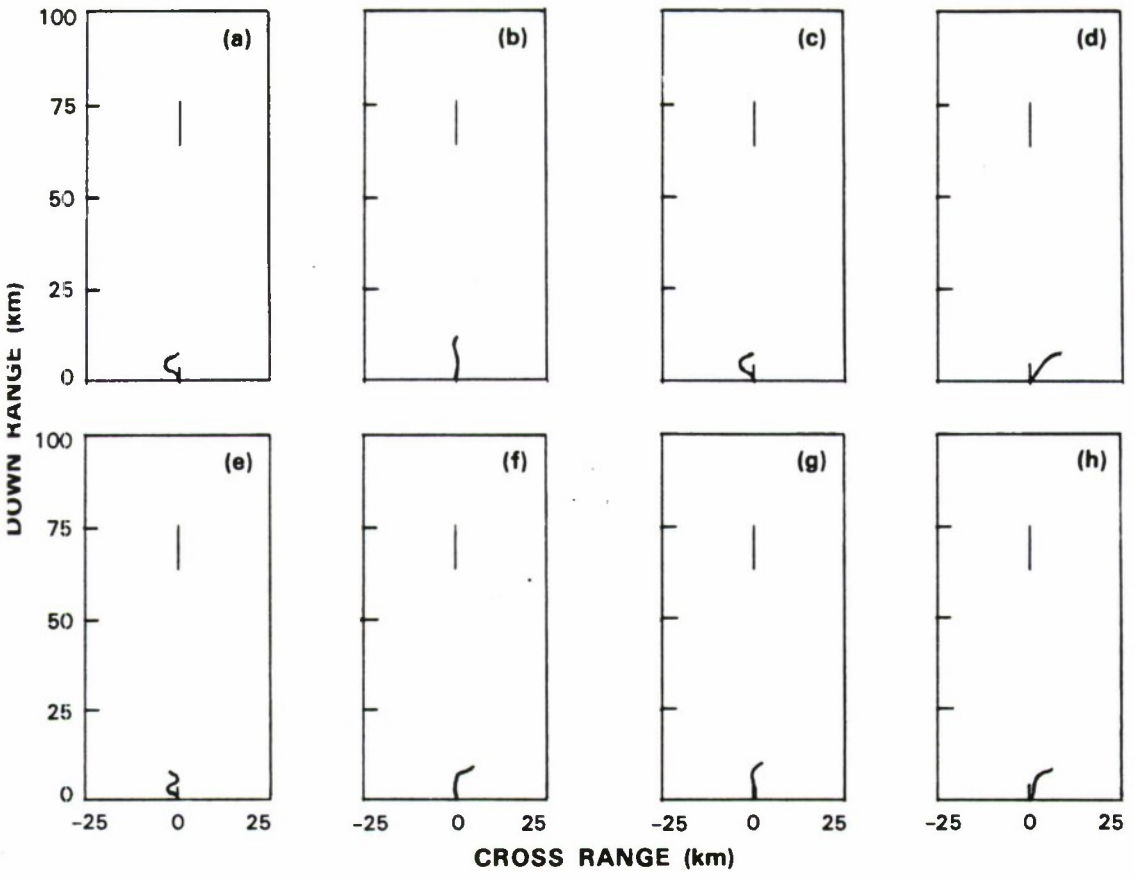

Figure 11. Optimal sensor maneuvers for various degrees of a priori knowledge, as listed in Table II. The plots are grouped into pairs, wherein the left member shows the optimal maneuver for target position estimation and the right member shows the optimal maneuver for target velocity estimation.

third local minimum at a very short maneuver period, associated with a relatively poor measurement accuracy. From this plot one must suppose that Olsder's minimization procedure was probably not trapped near the false local minimum at the short period but instead found a trajectory near one of the two nearly equal minima at a maneuver period equal to the 40-s observation time. The minimum position bound of 2.5 km obtained with the parameterized curves (Figure 3) agrees well with the value of 2.3 km given by Willman's equation [Equation (3.3)], with an angle standard deviation σ_a of 0.3°, a range R of 70 km, a sensor velocity v of 0.3 km/s, a sample interval T_s of 1 s, and an observation time T_o of 40 s. As a consequence of the assumption that the target has zero acceleration and zero radial velocity, the bounds on the range accuracy, shown in Figure 3, and the velocity accuracy, Figure 4, are unreasonably optimistic.

The plots tabulated in Table II show the bound contours for several levels of *a priori* information. The most optimistic results are obtained for a target whose range rate and acceleration are known almost exactly. Similar contours appear in Figures 5 and 6 for a target with a less well-known velocity and acceleration, but the velocity measurement optimization shows there that the sensor gains some advantage by moving cross range at an average velocity of 0.3 km/s – 0.07 km/s = 0.23 km/s, as shown in Figure 11(d). When the *a priori* information is reduced to the more reasonable level of a 0.4-km/s standard deviation for the velocity and a 4-g standard deviation for the acceleration, the contours shown in Figures 7 and 8 are obtained, and the optimal maneuvers are shown in Figures 11(e) and (f). When finally the *a priori* information is relaxed to the point where it is quite meaningless, one finds the behavior shown in Figures 9 and 10, with the optimal maneuvers given in Figures 11(g) and (h). While it would be pleasing if a trend in the optimal maneuver parameters could be found, none is apparent. Only the obvious conclusion, that the error bounds increase, from 2.5 km and 0.05 km/s to 9.8 km and 0.56 km/s as the *a priori* distributions grow broader, can be drawn. There appears to be little point in attempting to estimate the range rate of the target after only 40 s of observation time, except when its prior standard deviation is as much as 0.56 km/s, since the least achievable *a posteriori* velocity standard deviation is little different from the *a priori* standard deviation.

In Table III are shown the optimal sensor maneuver velocity Δv and maneuver period T_m found by exhaustive search for several different measurement situations. The geometries for the 70-km range are as shown in Figure 2, and the 200-km ranges have similar configurations. For position measurement, if the target is inbound at 70 km, inbound at 200 km, or crossing at 70 km, the optimal maneuver for a 40-s observation time is a weave with period of about 30 s. The situation differs somewhat for velocity measurement, where the period of the weave remains at about 40 s whether the target is at 70-km range or at 200-km range but, in the case of the nearer inbound target, less of the sensor's velocity is devoted to maneuvering and the sensor moves cross range at an effective velocity of 0.3 km/s – 0.17 km/s = 0.13 km/s while executing a smaller weave. The entries for the observation times of 20 s and 120 s show the dependence of the optimal trajectory on the time interval after which the best measurement is sought. The sensor speed devoted to maneuvering remains equal to the total speed of the sensor, but for the 20-s observation time the sensor completes nearly 1-1/2 cycles rather than 1-1/3 cycles for 40- and 120-s observation times. It is not clear why the optimal number of cycles should depend on the observation time in this way.

TABLE III

Optimization Results for Various Target Geometries, State Vector Components, and Observation Times, for the Parameters Given in Table I

Target State (km)	Optimization Objective	Observation Time (s)	Best Δv (km/s)	Best T_m (s)	Resulting Bound
70 inbound	position	40	0.30	29	7.3 km
70 crossing	position	40	0.30	29	7.3 km
200 inbound	position	40	0.30	27	36 km
70 inbound	velocity	40	0.17	42	0.32 km/s
70 crossing	velocity	40	0.29	42	0.25 km/s
200 inbound	velocity	40	0.30	42	0.40 km/s
70 inbound	position	20	0.30	13	12 km
70 inbound	position	120	0.24	64	0.62 km
200 inbound	position	120	0.30	88	13.7 km/s

4. ERROR BOUNDS FOR SUBOPTIMAL SENSOR TRAJECTORIES

The sensor platform will not be able to optimize its trajectory for estimating the state of the target without knowing that state in advance, and one therefore needs a robust maneuver trajectory. The sensor platform can, however, move in a way that provides the best estimate of the target's state under some worst-case situation. It is therefore important to determine how sensitive the error bounds on estimates of the state of the target are to mismatches between the sensor platform's actual trajectory and the optimal trajectory for a given target trajectory.

Figures 13 through 23 show how the error bounds on estimates of the range and velocity of a target vary as a function of elapsed time, for six different target trajectories and for various sensor maneuvers. The six target trajectories, shown in Figure 12(a-f) and tabulated in Table IV, are at similar ranges and speeds but vary in direction and acceleration. Trajectories (a-c) are crossing and (d-f) are inbound. Of each group of three, one has zero lateral acceleration, one has 0.5-g lateral acceleration, and one has 1-g lateral acceleration. The key to the plots in Figures 13 to 23 is given by the parameters in Table V and by the markings on the subplots in Figure 12. The optimal maneuver is the same for position measurement of an inbound target at either 70- or 200-km range or for a crossing target at 70 km, and the combinations that would be redundant are not tabulated. The plots show that range and velocity measurement performance against crossing targets is better than that for inbound targets, that for crossing targets the target's actual acceleration has little effect on the bound, but that performance is better against inbound targets

TABLE IV

Parameters Describing the Motions of Targets at 70-km Range

	Initial Position		Initial Velocity		Constant Acceleration	
Plot	x (km)	y (km)	x (km/s)	y (km/s)	x (km/s^2)	y (km/s^2)
(a)	-18	70	0.3	0	0	0
(b)	-18	74.5	0.3	-0.3	0	0.005
(c)	-18	79	0.3	-0.6	0	0.01
(d)	0	88	0	-0.3	0	0
(e)	4.5	88	-0.3	-0.3	0.005	0
(f)	9	88	-0.6	-0.3	0.01	0
(g)	0	88	0.3-km/s speed, initially inbound, 2°/s turn rate			

The first column refers to the plots in Figure 12. To obtain the positions of the targets at a range of 200 km, y components of the initial positions are increased by 130 km.

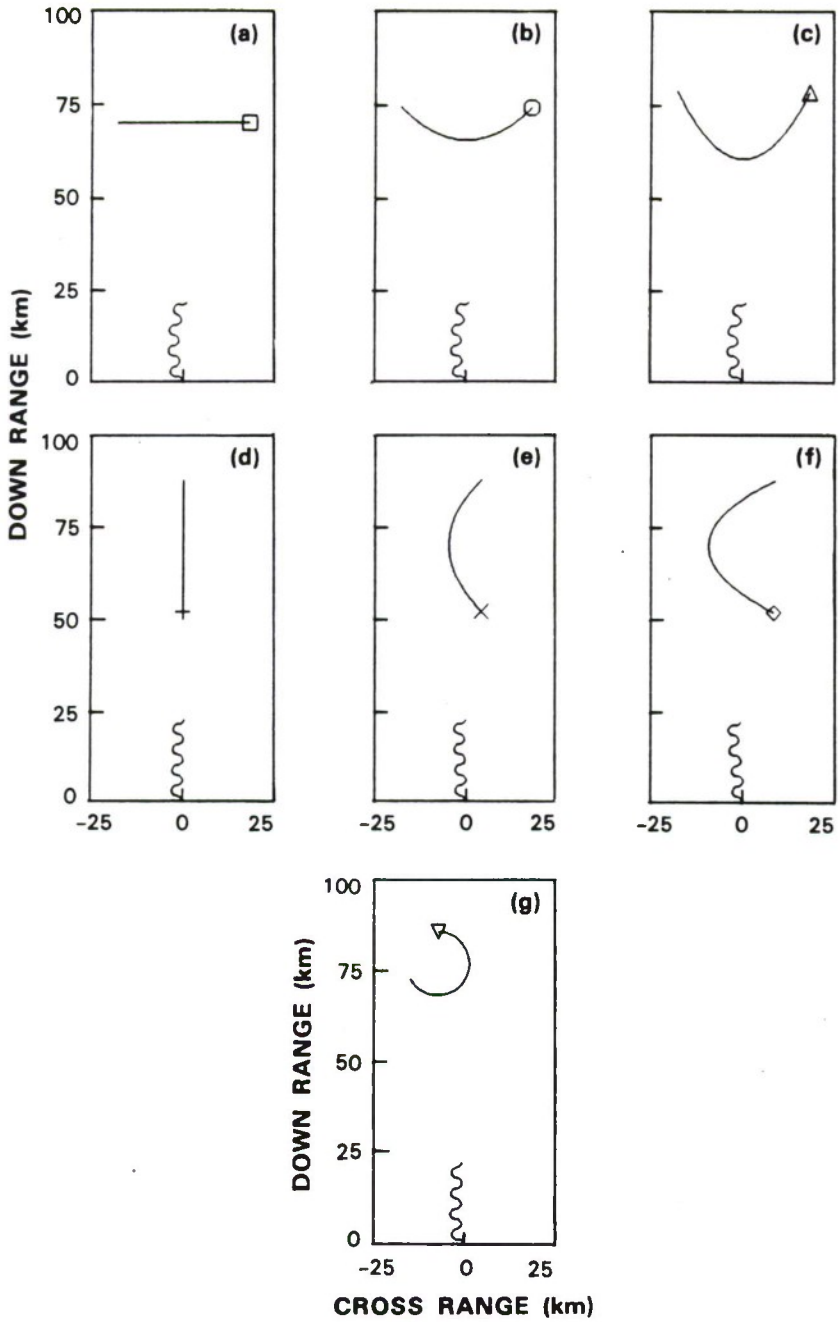

101776-12

Figure 12. Illustration of target trajectories used in bound calculations, with parameters as shown in Table IV. The symbol marks the position of the target at the end of the observation time and is keyed to the subsequent plots in this report. The sensor speed is 0.3 km/s with a maneuver velocity of 0.3 km/s and a cycle time of 30 s. The total time shown here is 120 s, and all distances are in kilometers.

that accelerate laterally than against straight-line inbound targets. These observations lead to the intuitive notion that lateral motion by the target in effect adds to the lateral motion of the sensor to increase the baseline from which the range to the target is estimated.

The figures also illustrate that the measurement accuracy remains relatively poor until the designated observation time for which the trajectory was optimized is reached. Thus, if the maneuver is optimized for an observation time of 120 s (Figures 20 and 21), the bound is quite large for intermediate times, but at 120 s the limit is smaller than it would be if the sensor path were optimized for a shorter period. The optimization for a 20-s observation time illustrates the extreme where the trajectory is optimized for a very short observation time, leading to better performance at 20 s than do the longer observation times but to much poorer performance thereafter. Shorter observation times permit acceptable results more rapidly and minimize the degree of possible mismatch between the paraboblic model of the target's trajectory and the target's true trajectory, but too short a maneuver period can result in a very poor target state estimate.

The sensitivity of the bound to mismatches between the target state for which the sensor maneuver was optimized and the true target state does not seem great enough to merit much concern. The position and velocity estimates in Figures 13 through 18 illustrate the variations of the bound for several combinations of model and true states. The position and velocity error bounds do appear to be sensitive to whether the sensor trajectory was optimized for position or velocity measurement, with degradations of about a factor of 2 for a mismatch. The velocity measurement bounds also show some sensitivity to whether the trajectory is optimized for targets at 70- or at 200-km range.

The quality of the estimates can be improved by increasing either the rate at which independent samples of the bearing are taken (Figure 22) or by improving the accuracy of the measurements (Figure 23). The extent of the observed improvement is in line with the notions expressed earlier that the bound on the standard deviation of the estimate should be inversely related to the number of samples taken during the observation time and proportional to the standard deviation of the angle measurements. Thus increasing the sample rate by a factor of 10 reduces the bound by a factor of about 3, and improving the angular accuracy by a factor of 10 reduces the bound by a factor of 10.

TABLE V

Parameters for Figures 13 Through 21

Case	Target Range (km)	Sample Rate (Hz)	Angle Standard Deviation (deg)	Target Starting Range (km)	Measurement	Observation Time (s)	Figure
1	70	1	0.3	70	position	40	13
2	70	1	0.3	70	velocity	40	14
3	70	1	0.3	200	velocity	40	15
4	200	1	0.3	70	position	40	16
5	200	1	0.3	70	velocity	40	17
6	200	1	0.3	200	velocity	40	18
7	200	1	0.3	70	position	20	19
8	70	1	0.3	70	position	120	20
9	200	1	0.3	200	position	120	21
10	200	10	0.3	70	position	40	22
11	200	1	0.03	70	position	40	23

The fifth through eighth columns specify the conditions for which the sensor's trajectory was optimized. The maneuver velocities and periods for the sensor trajectories are summarized in Table III. The figures specified in column eight show the bounds for the target's range and range rate. The bottom two rows have parameters different from those specified in Table I and are included for comparison.

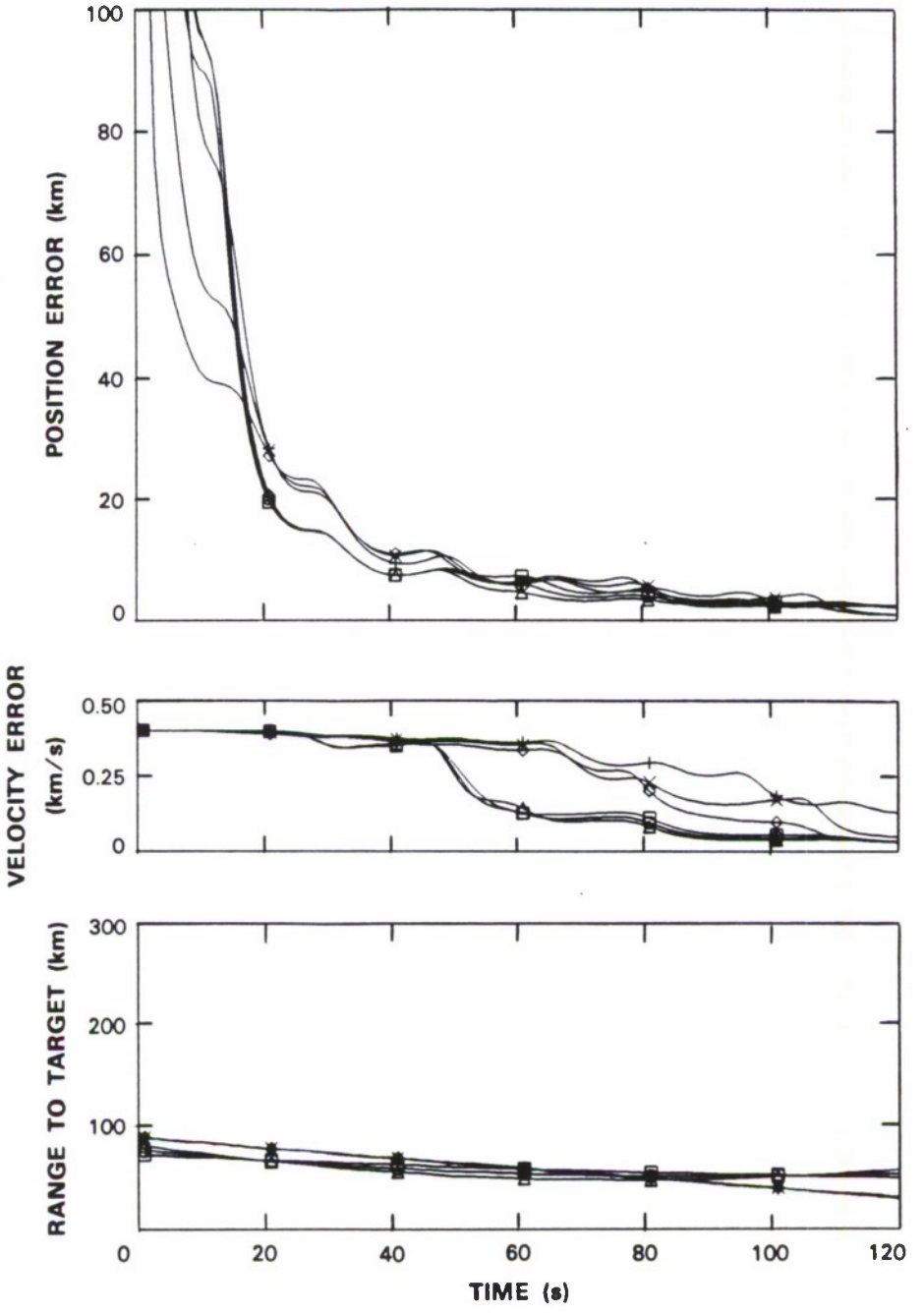

101776-13

Figure 13. Cramér-Rao bound vs tracking time for Case 1, Table V.

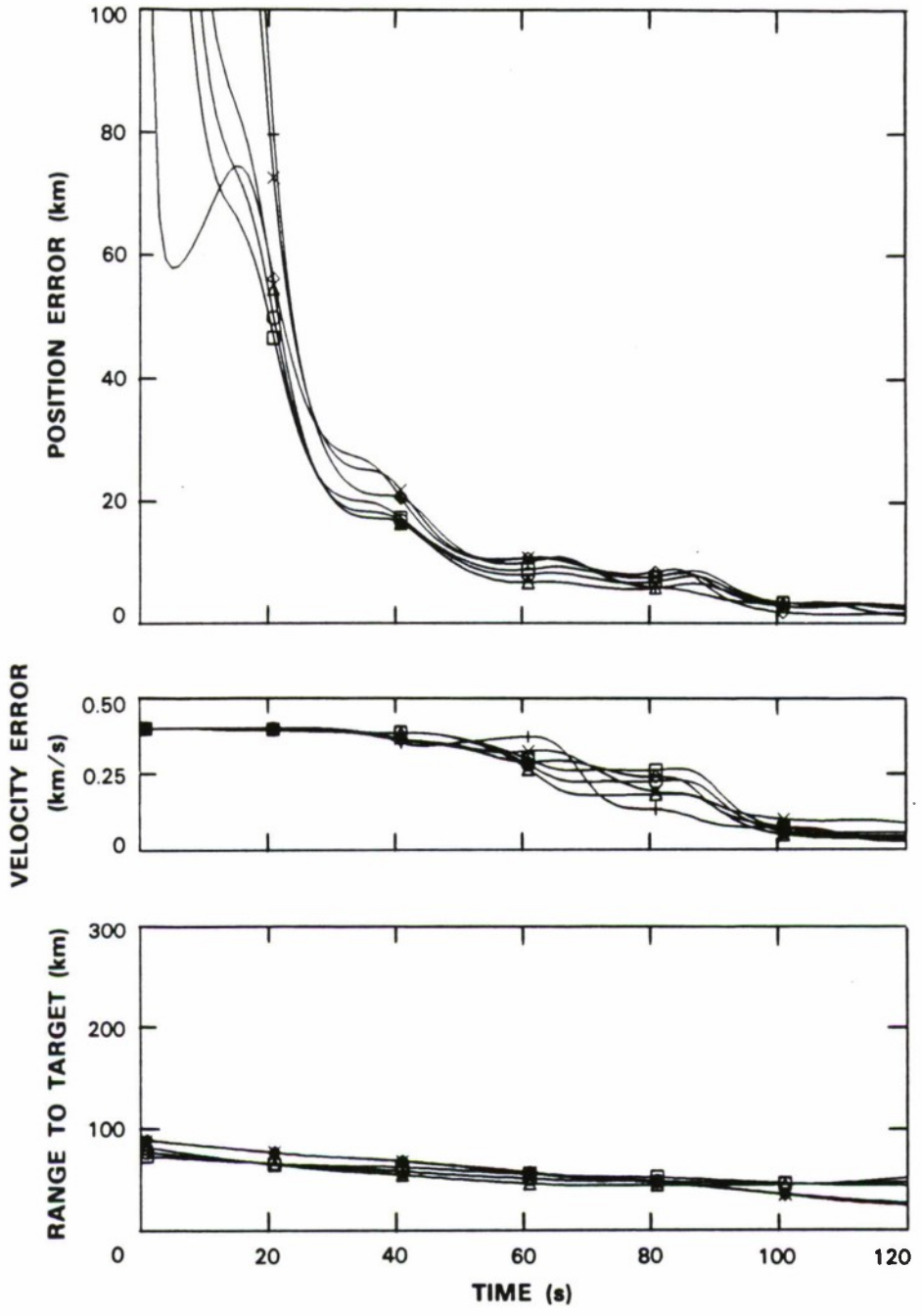

101776-14

Figure 14. Cramér-Rao bound vs tracking time for Case 2, Table V.

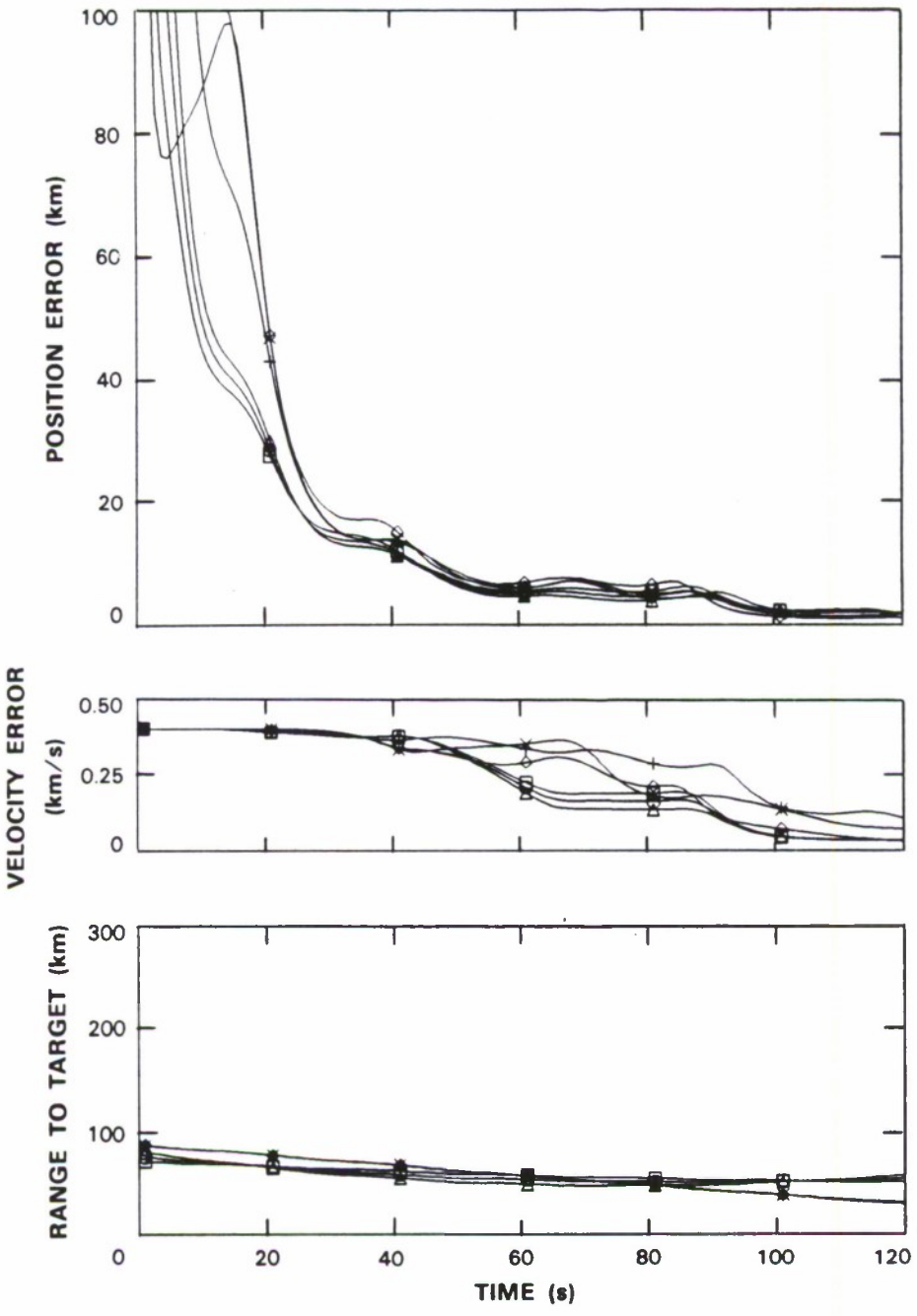

101776-15

Figure 15. Cramér-Rao bound vs tracking time for Case 3, Table V.

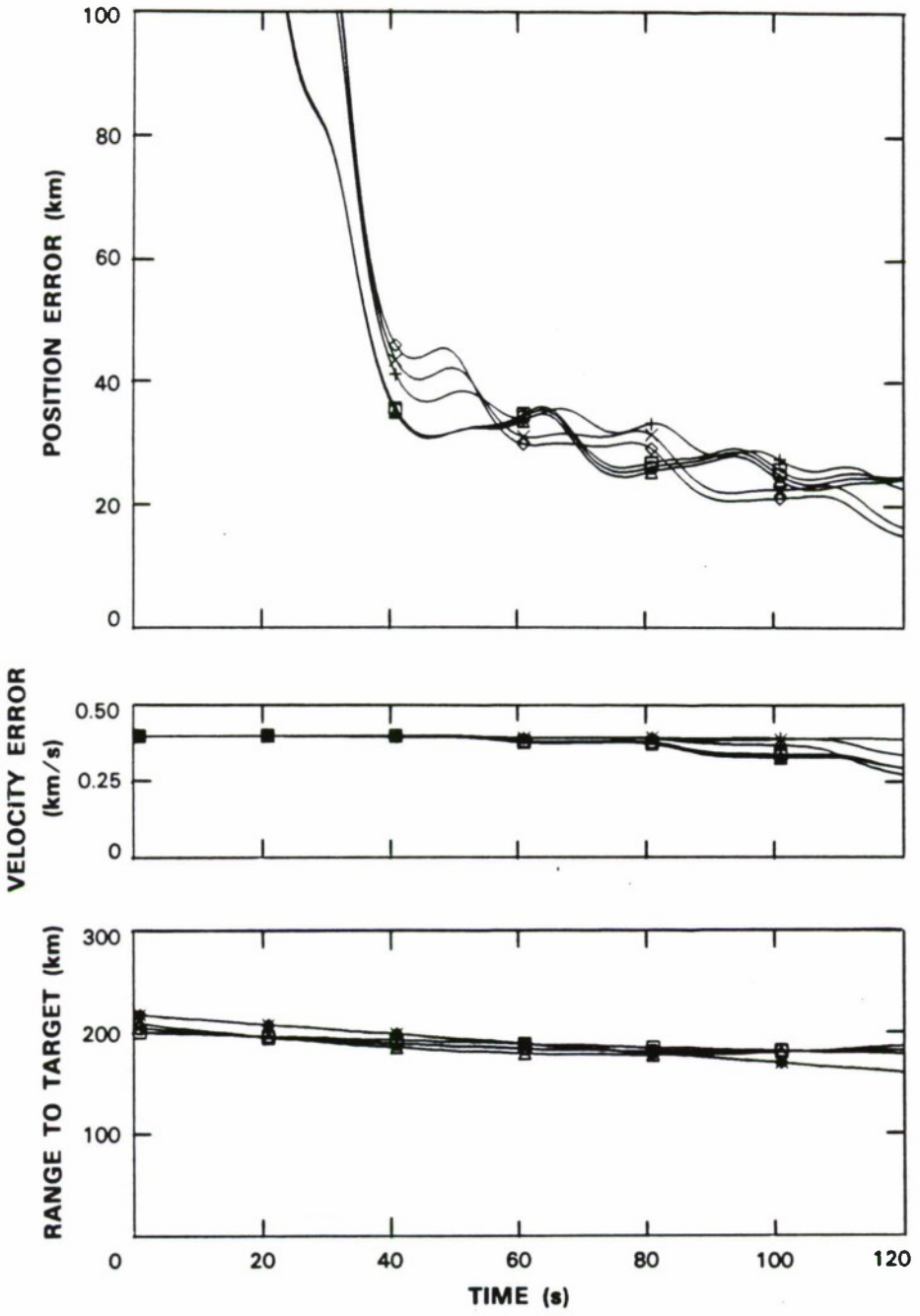

Figure 16. Cramér-Rao bound vs tracking time for Case 4, Table V.

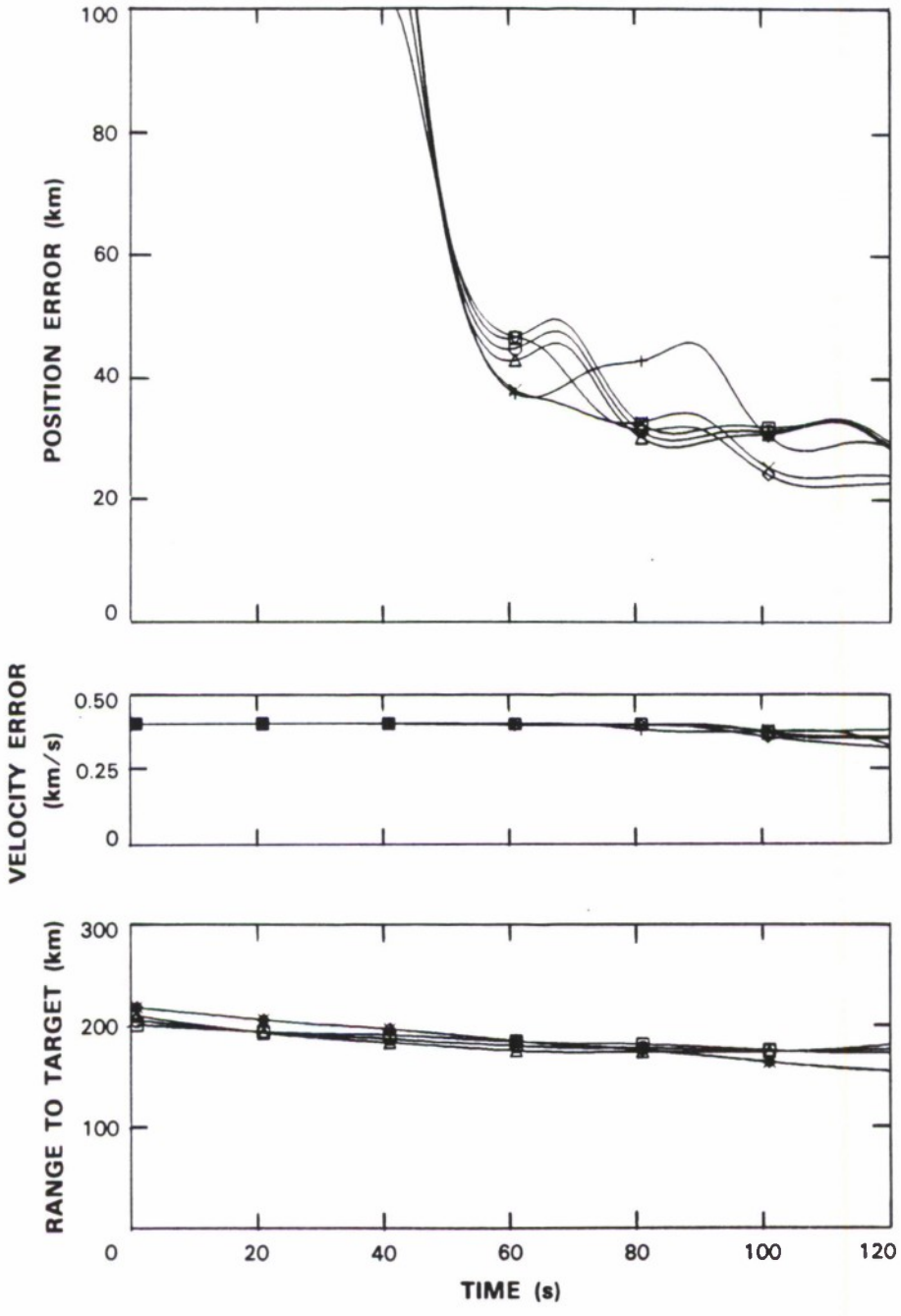

101776-17

Figure 17. Cramér-Rao bound vs tracking time for Case 5, Table V.

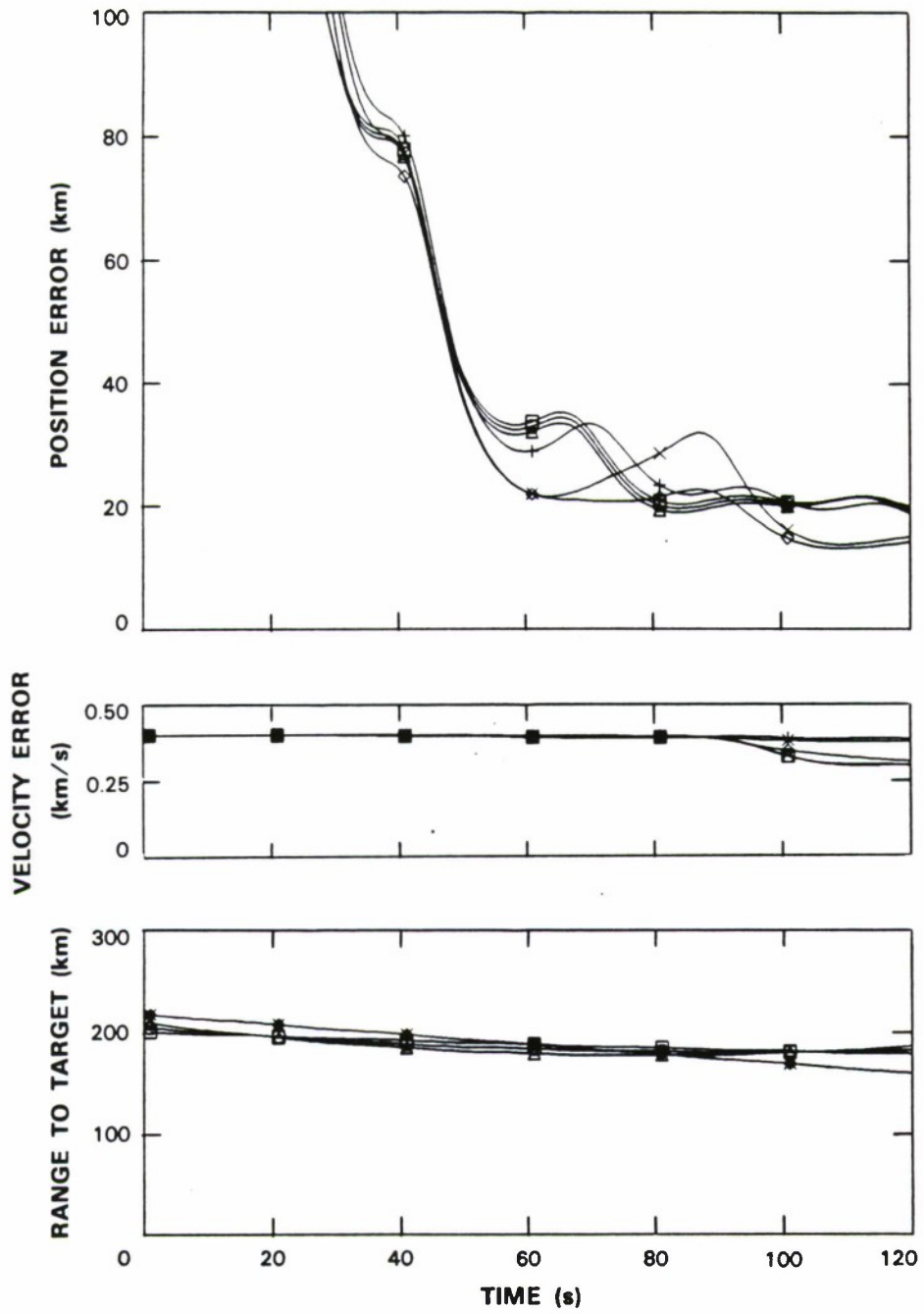

Figure 18. Cramér-Rao bound vs tracking time for Case 6, Table V.

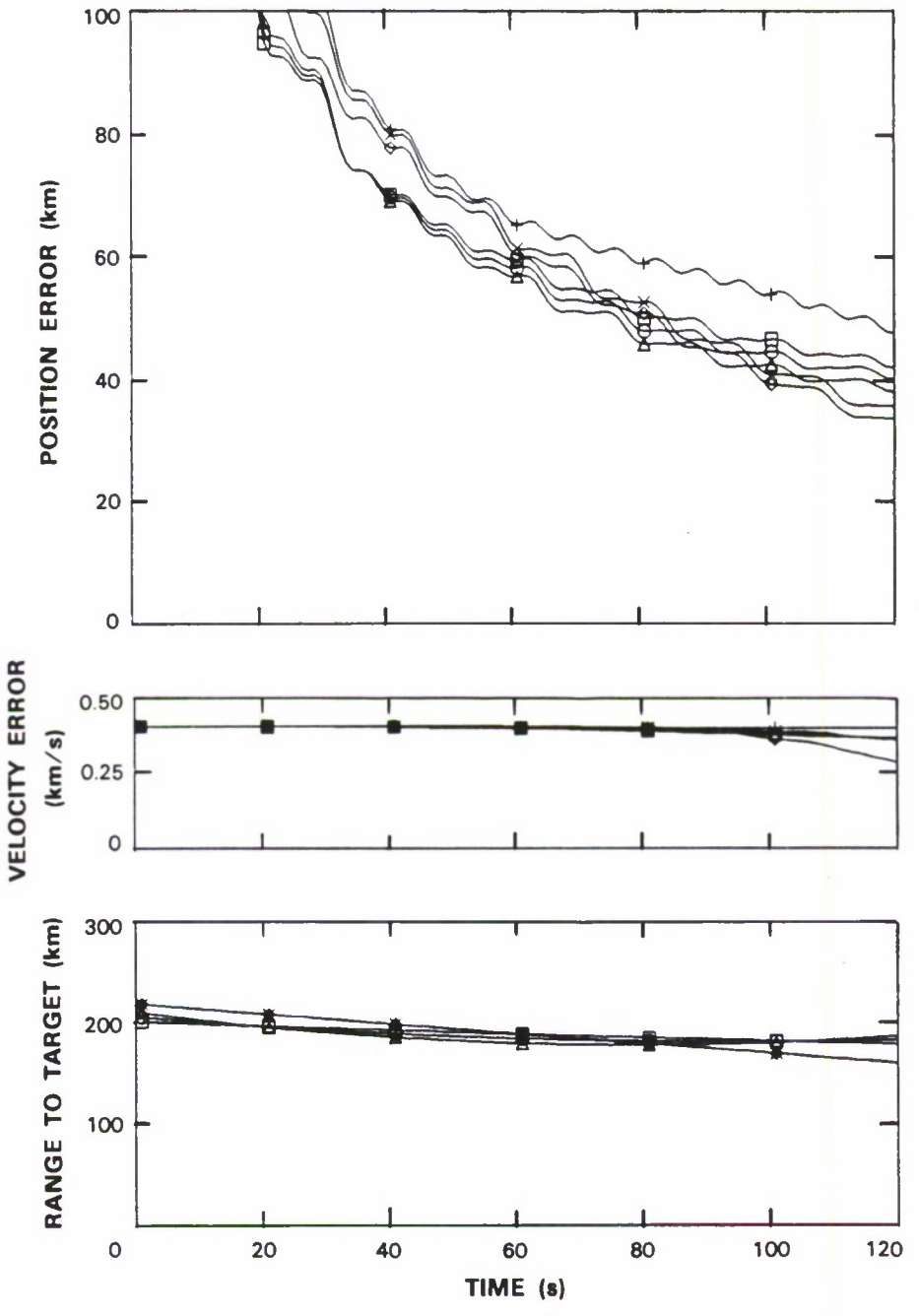

101776-19

Figure 19. Cramér-Rao bound vs tracking time for Case 7, Table V.

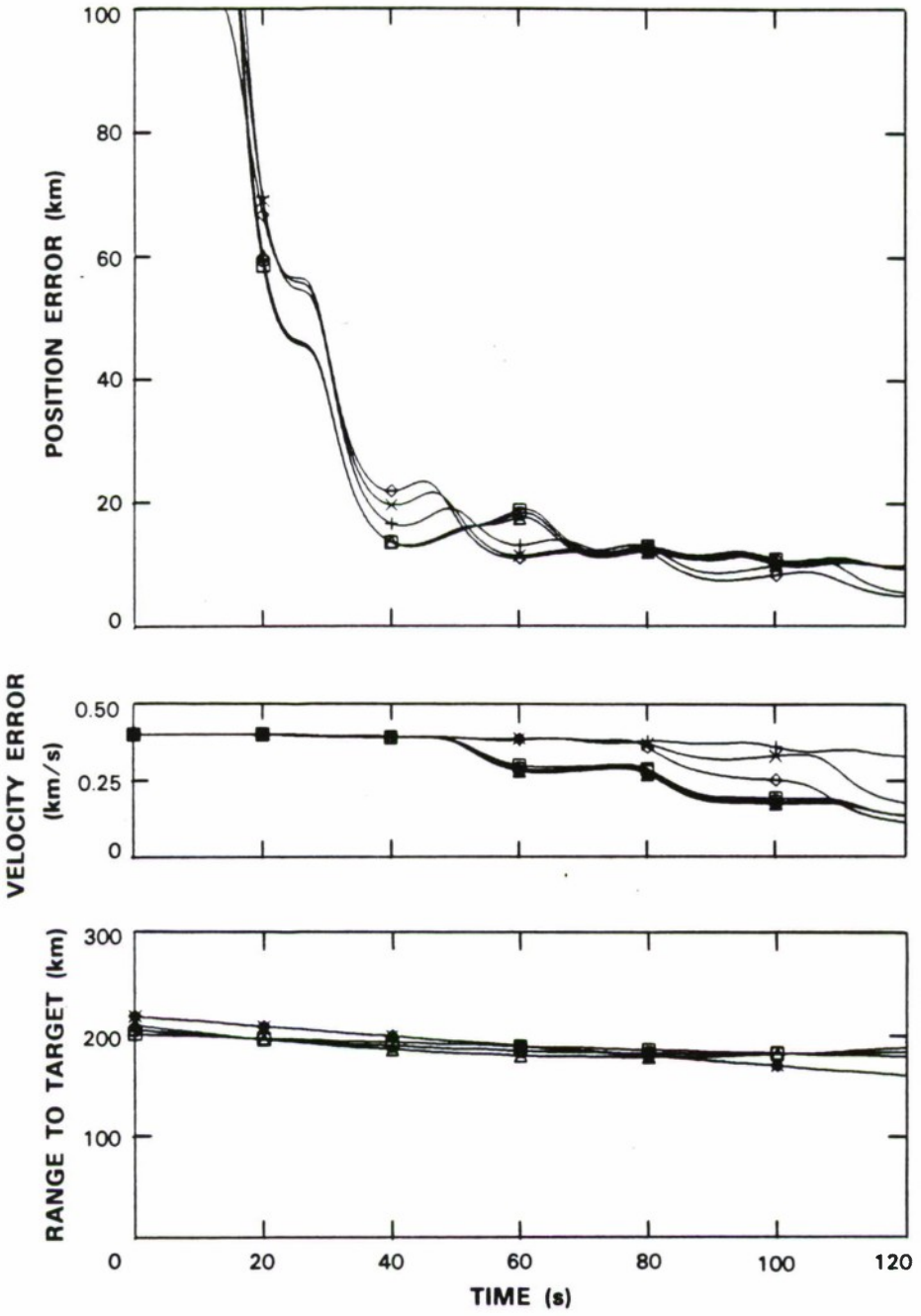

101776-20

Figure 20. Cramér-Rao bound vs tracking time for Case 8, Table V.

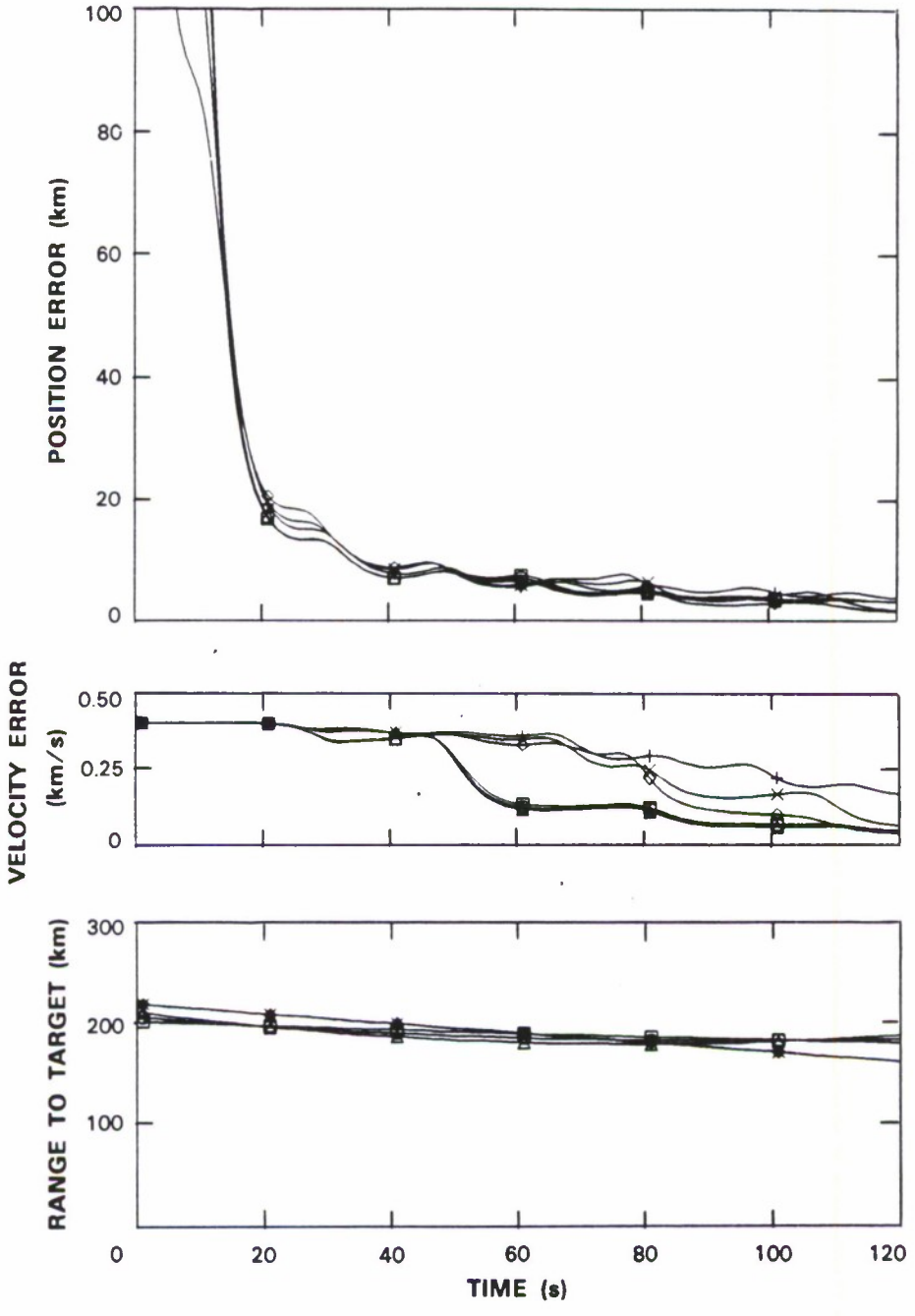

101776-21

Figure 21. Cramér-Rao bound vs tracking time for Case 9, Table V.

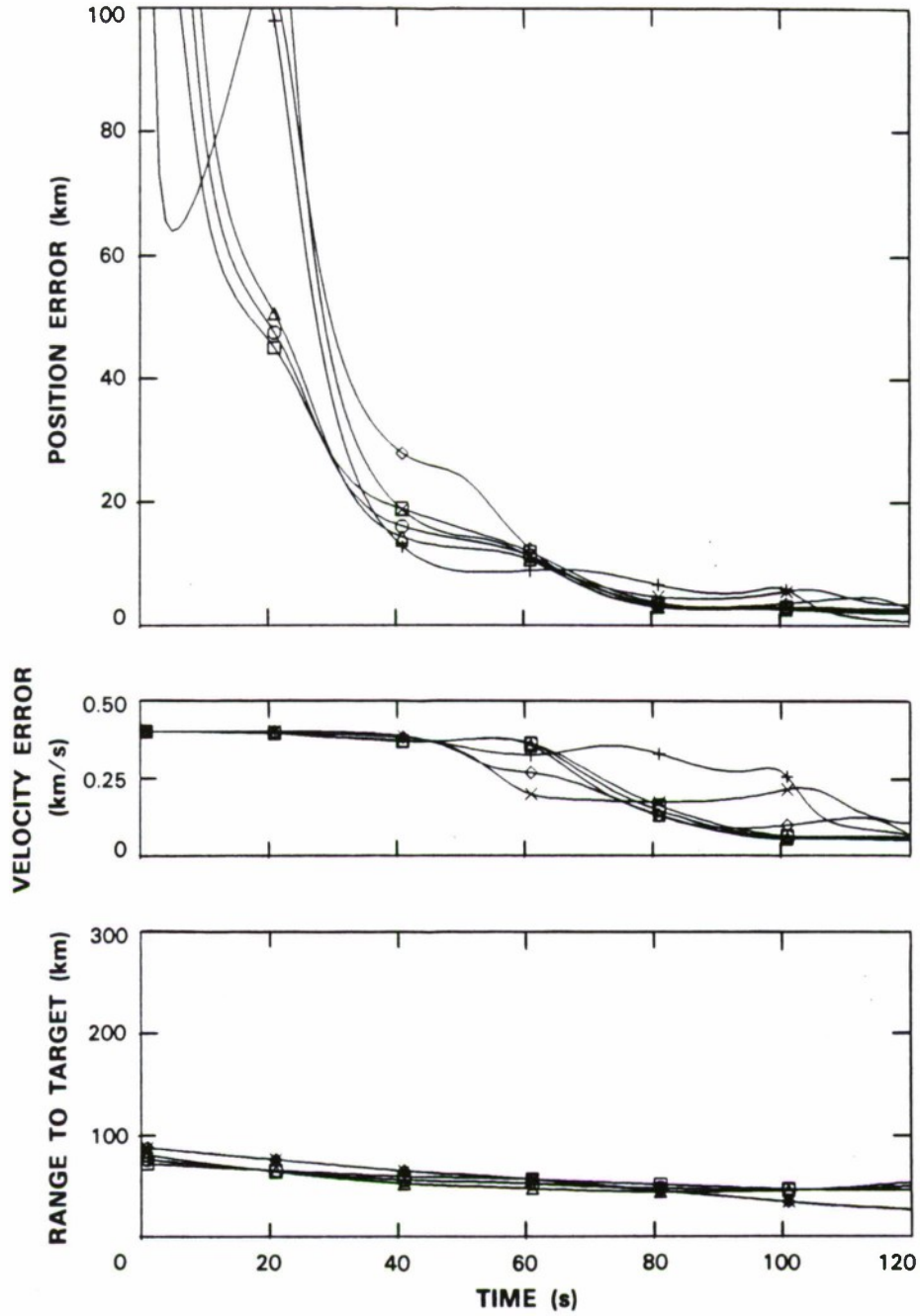

101776-22

Figure 22. Cramér-Rao bound vs tracking time for Case 10, Table V.

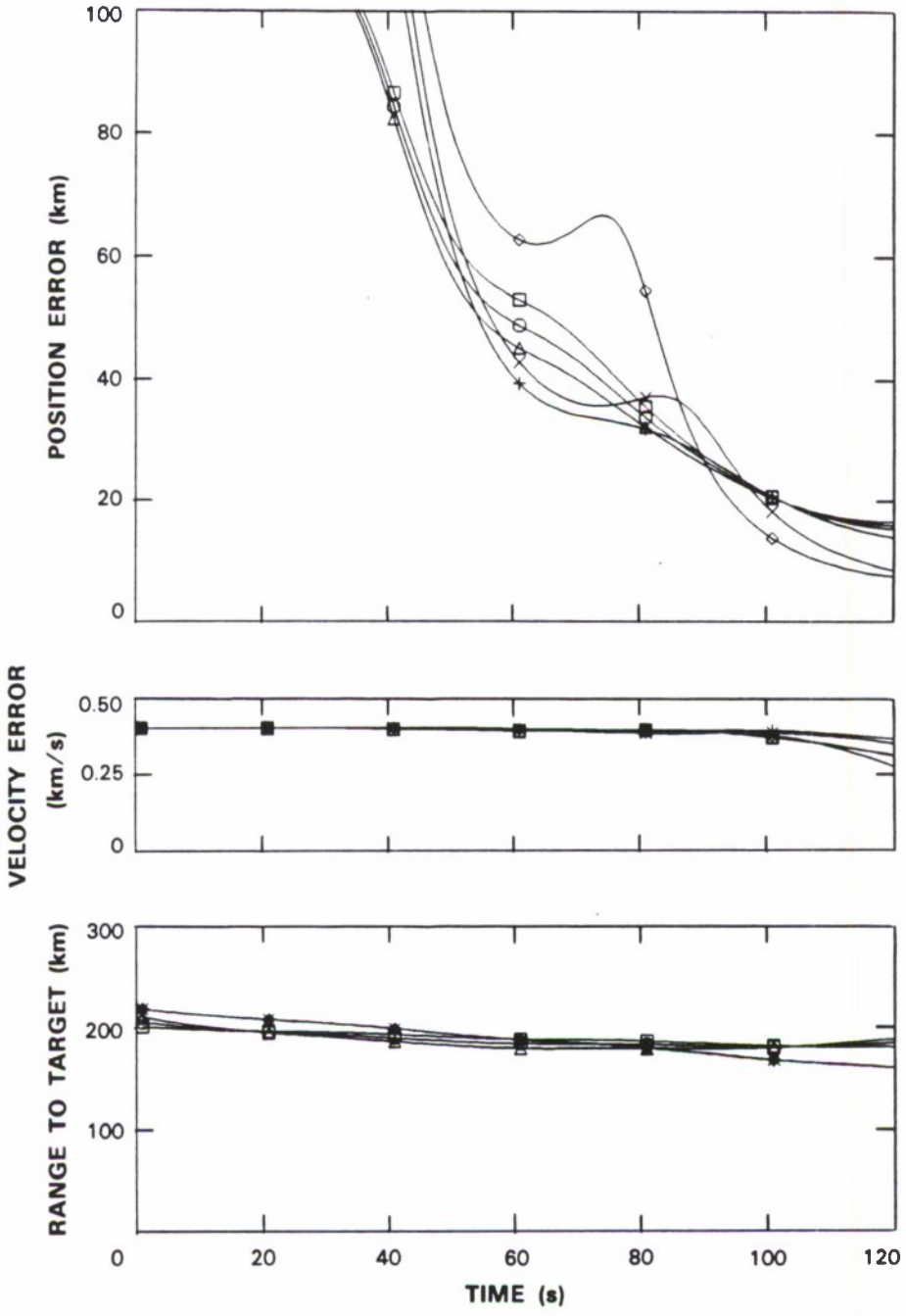

101776-23

Figure 23. Cramér-Rao bound vs tracking time for Case 11, Table V.

5. MAXIMUM *A POSTERIORI* PROBABILITY TARGET TRACKS

Tests of a maximum *a posteriori* probability (MAP) estimator showed performance at the level given by the Cramér-Rao bounds. They also disclosed serious divergences in the estimates with targets whose trajectories differed significantly from the models on which the estimators were based. The MAP estimator of the target state was implemented using an iterative least-squares method described in Reference 8 and in Reference 24, pp. 187-190. The equations for the iterative least-squares algorithm are given in the Appendix. The *a priori* distribution of the target state at the time of the latest measurement was taken to be zero-mean Gaussian with a velocity standard deviation of 0.4 km/s and an acceleration standard deviation of 4 g, except where the target model was linear, in which case the *a priori* standard deviation of the acceleration was in effect zero. Although a zero-mean Gaussian is perhaps not the most plausible distribution, it has the advantages of being handled easily and of leading to estimation algorithms that apparently converge to global maxima of the probability. Tracks were obtained by appending new measurements to the list of previous measurements and running the iterative least-squares algorithm on the updated data starting with the previous state estimate as the new initial guess. The first point in the track was obtained once 20 bearing measurements had been collected. The estimators showed no dependence on the initial guess and appeared to be finding the global minimum of the error.

The plots in Figures 24 to 33 show how the actual performance of the estimator depends on the target model and on the degree of mismatch between the model and the target's actual motion. The figures show Monte-Carlo simulations results for 50 runs of each of two target models, linear and parabolic, and for three actual target trajectories, linear, parabolic, and circular, in the combinations listed in Table VI. These target trajectories correspond to entries (d), (c), and (g) in Table IV. The figures are grouped into pairs, with Figures 24, 26, 28, 30, and 32 showing the combined Monte-Carlo results and with Figures 25, 27, 29, 31, and 33 showing single sample runs. The combined results show the Cramér-Rao bound standard deviations for target range, radial velocity, and radial acceleration errors as solid curves, the estimator biases as short-dashed curves, and the estimator rms errors as dotted curves. The iterative least-squares algorithm computes an estimate of the Fisher information matrix as a by-product, and estimated bounds computed from the estimates of the Fisher information matrix from a single sample run are shown as long-dashed lines. Since the Cramér-Rao bounds account for the uncertainty in the *a priori* target state as well as the random errors in the data, the bounds should be compared with the combined bias and rms errors from the Monte-Carlo simulations. The Cramér-Rao bound is excluded from the circular target plots in Figure 32 because the bound as calculated is not appropriate to such a mismatched model. The sample runs in Figures 25 and 27 were plotted for target trajectories at 45° to the initial line of sight to the sensor in order to avoid overlap and thus to make the tracks clearer.

TABLE VI Key to Figures 24 Through 33		
Target Trajectory	**Target Model**	**Figures**
Linear	Linear	24 and 25
Linear	Parabolic	26 and 27
Parabolic	Linear	28 and 29
Parabolic	Parabolic	30 and 31
Circular	Parabolic	32 and 33

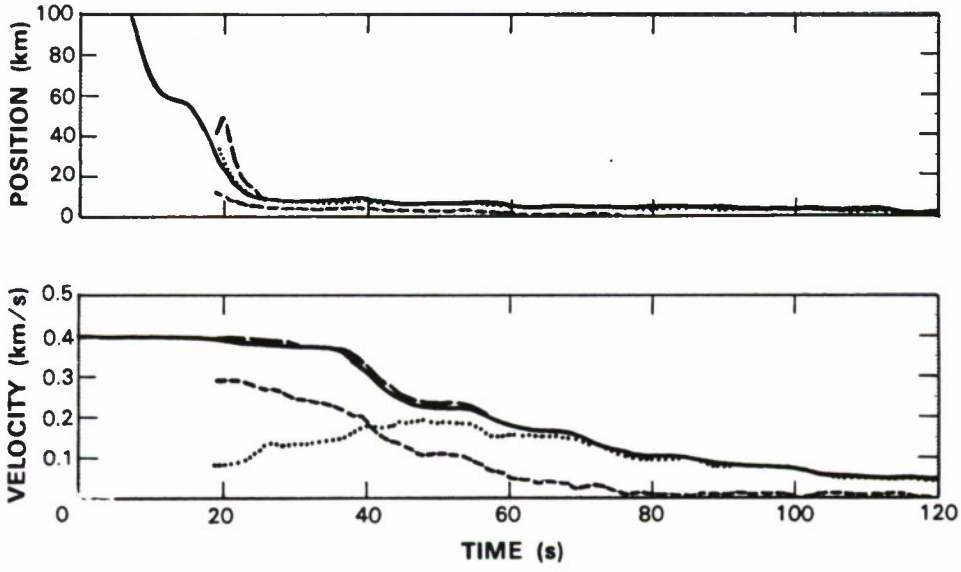

Figure 24. Monte-Carlo bias (dashed) and rms error (dotted) for a straight-line trajectory and target model.

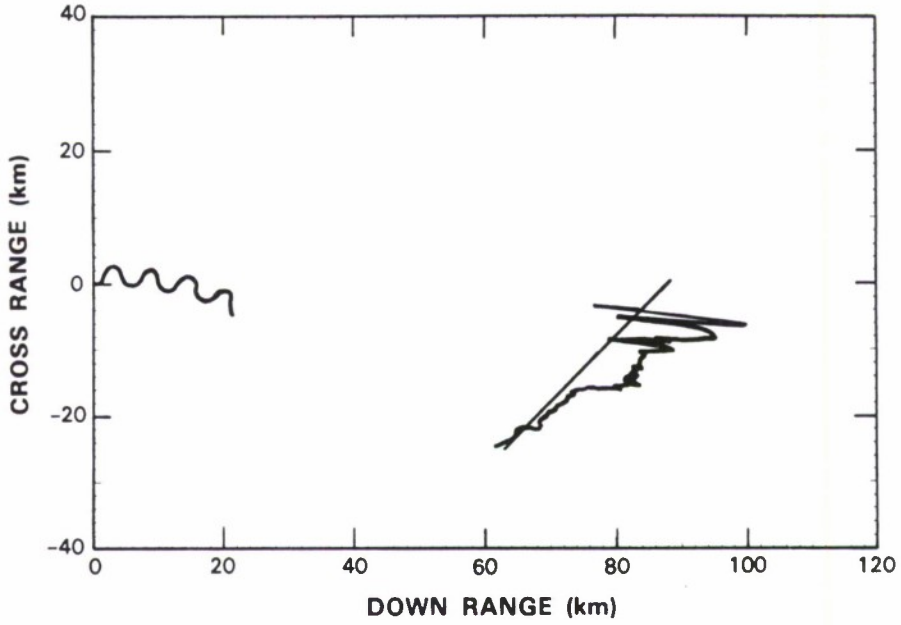

101776-25

Figure 25. Plan view of a single run with a straight-line target trajectory and model.

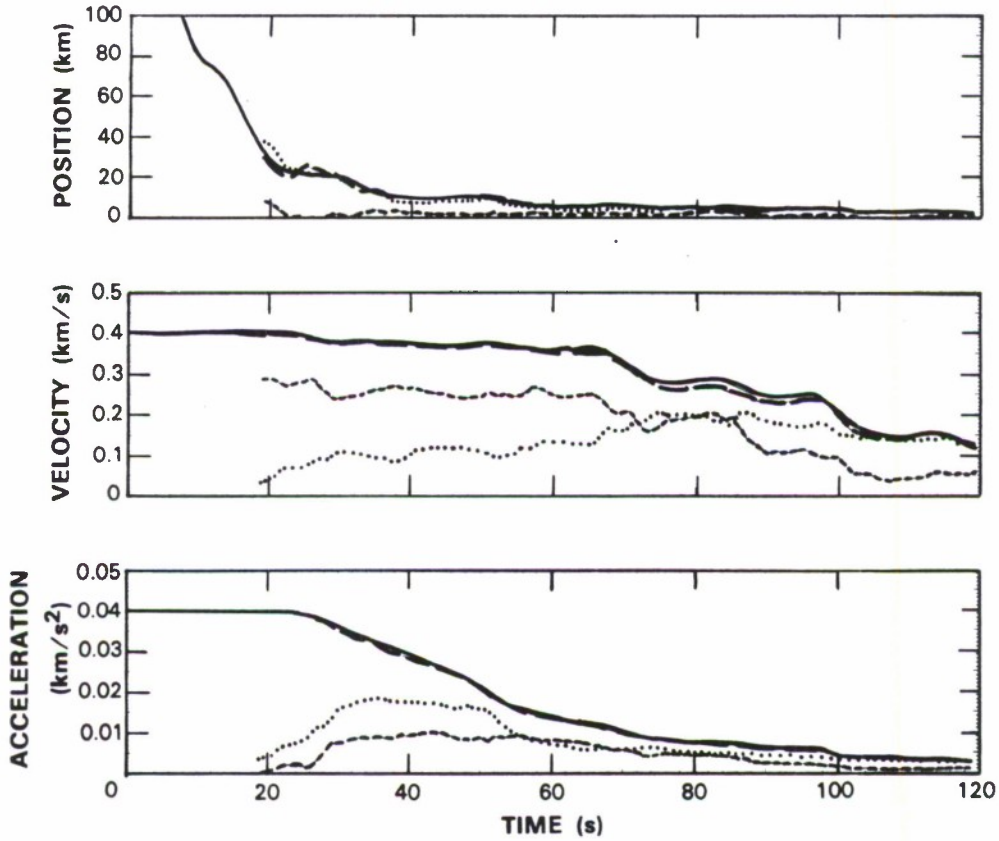

101776-26

Figure 26. Monte-Carlo bias (dashed) and rms error (dotted) with Cramér-Rao bound (solid) for a straight-line target trajectory but a parabolic trajectory model.

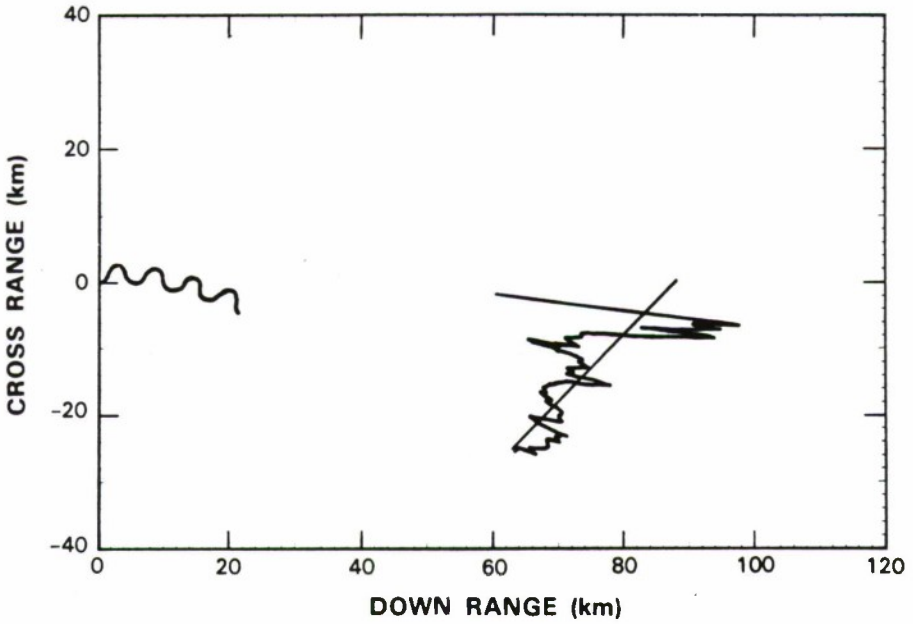

101776-27

Figure 27. Plan view of a single run with a straight-line target trajectory but a parabolic model.

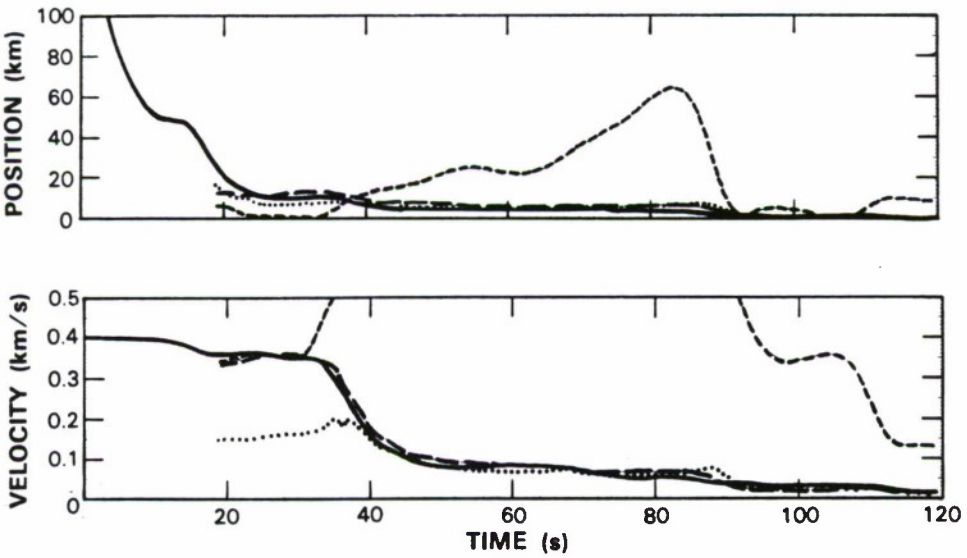

101776-28

Figure 28. Monte-Carlo bias (dashed) and rms error (dotted) with Cramér-Rao bound (solid) for a parabolic target trajectory but a straight-line target trajectory model.

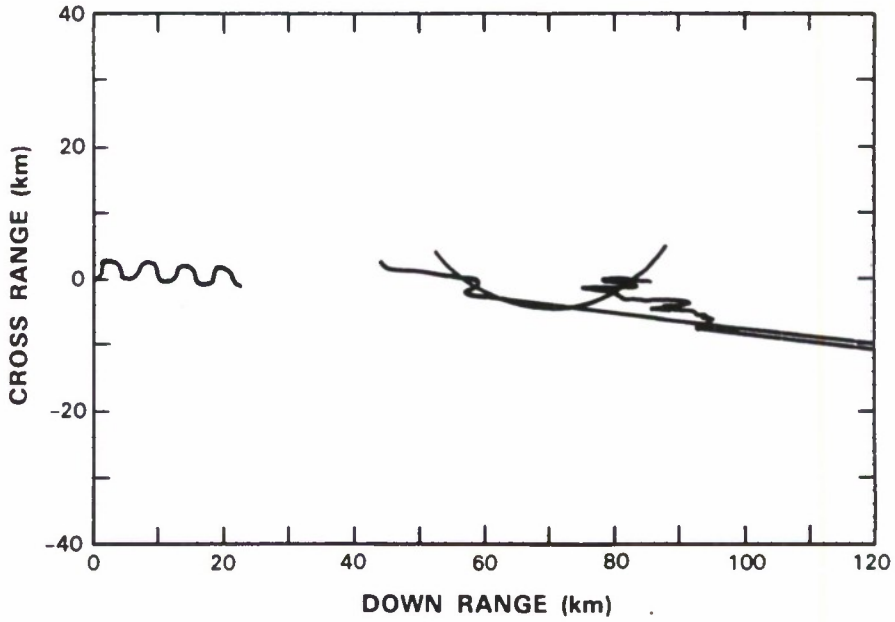

101776-29

Figure 29. Plan plot of a single run with a parabolic target trajectory but a straight-line target model.

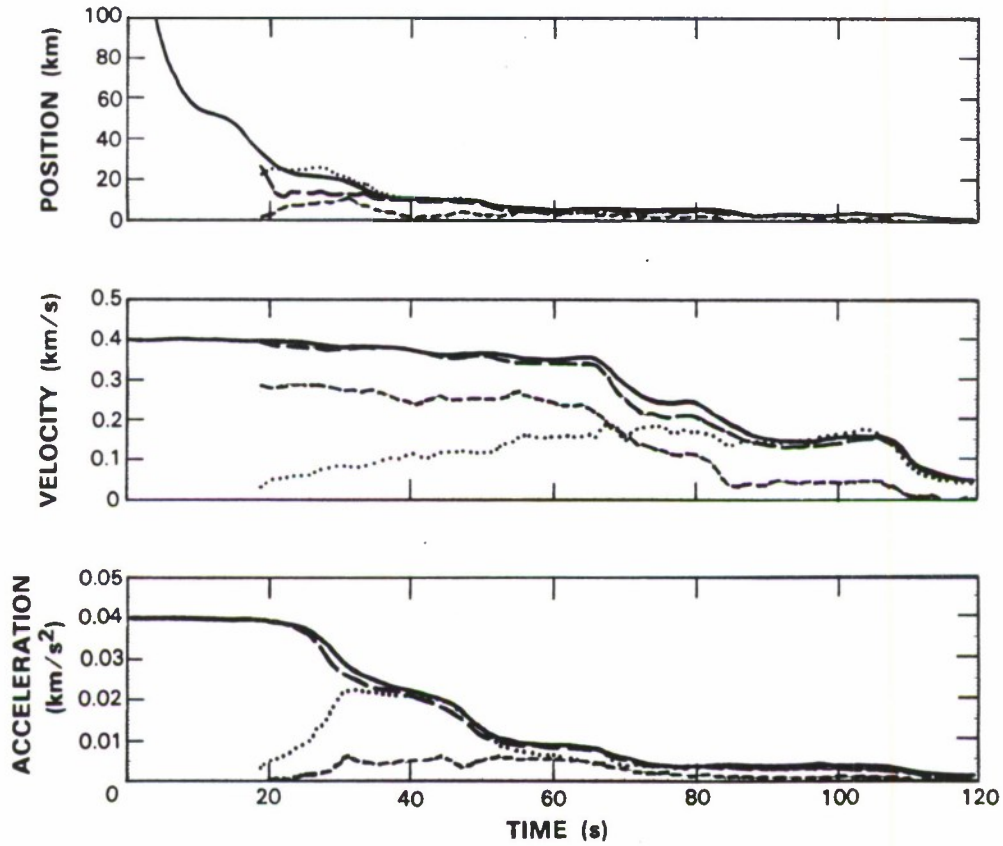

101776-30

Figure 30. Monte-Carlo bias (dashed) and rms error (dotted) with Cramér-Rao bound (solid) for a parabolic target trajectory and trajectory model.

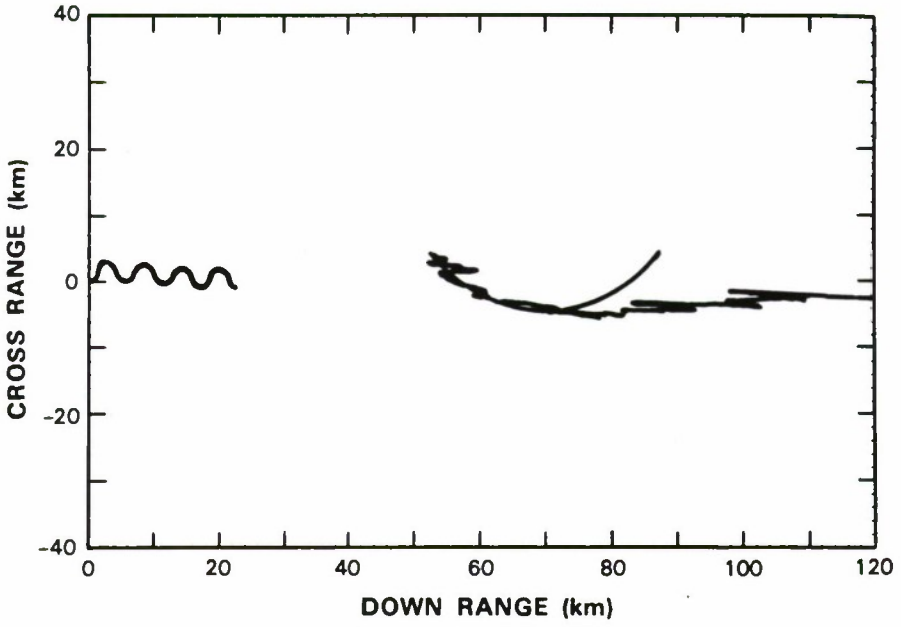

101776-31

Figure 31. Plan view of a sample run with parabolic target trajectory and model trajectory.

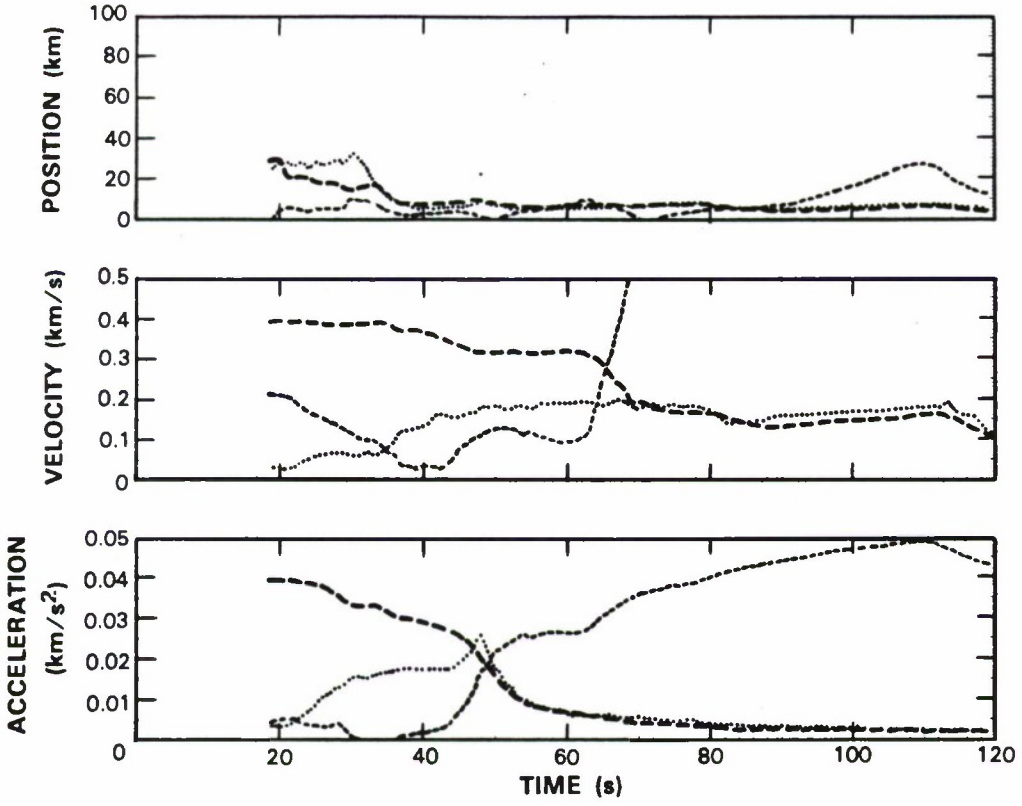

101776-32

Figure 32. Monte-Carlo bias (dashed) and rms error (dotted) for a circular target path but a parabolic target model.

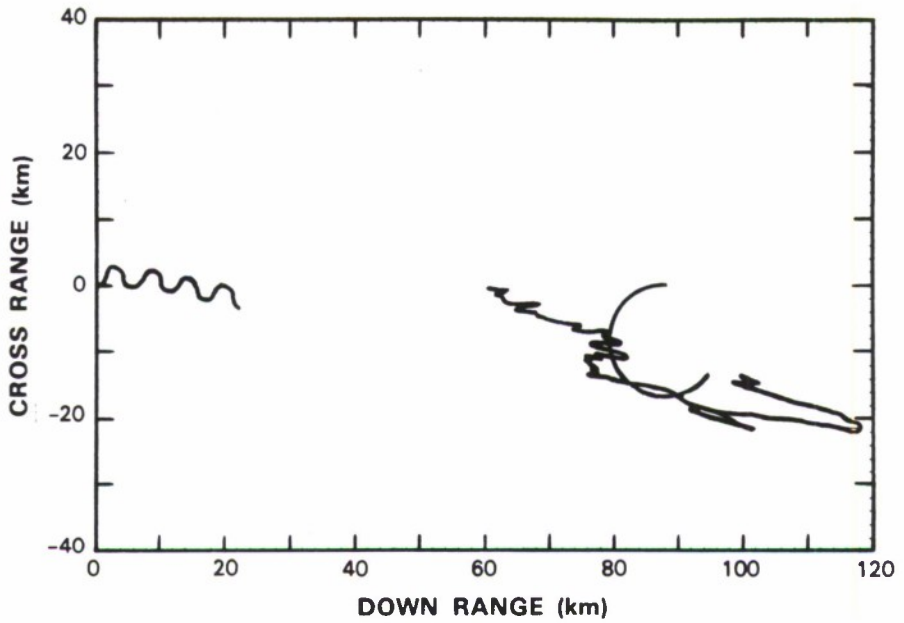

101776-33

Figure 33. Plan view of a single run with a circular target path but a parabolic target model.

Figures 24 and 26 show that the errors from a MAP estimator that incorporates the *a priori* knowledge that the target's acceleration is zero are smaller than the errors from an estimator that permits target acceleration, if the target is not in fact accelerating. The simulations also illustrate the impact on the estimation performance of discrepancies between the estimator's model of the target state and the actual motion of the target. Figures 24 and 25 and Figures 28 and 29 show the errors from estimators based on a constant velocity model of the target, as opposed to the constant acceleration model used in the other figures. A constant velocity estimator can be viewed as a constant acceleration estimator that happens to have definite *a priori* information that the target's acceleration is zero, and a mismatch occurs when that *a priori* information is incorrect. When the target's velocity is indeed constant, as in Figures 24 and 25, a constant velocity estimator is superior to an estimator based on a constant acceleration model of the target. However, if the target describes a curved path, as in Figures 28 and 29, the constant velocity estimates of the position and velocity diverge radically from the true values. In the case of a constant acceleration estimate applied to a target whose rate of turn is constant, shown in Figures 32 and 33, the errors show relatively small biases for the first 60 s, while the model and target do not differ greatly, but once the target begins to recede from the sensor platform the mismatched estimates diverge widely. The estimated Cramér-Rao bounds from a single sample run, shown as long-dashed curves in the figures, match the actual Cramér-Rao bounds very closely. In the cases of an accelerating target with a constant velocity model and of a circling target with a constant acceleration model, the estimates of the Cramér-Rao bound give good indications of the errors for the periods where the target's trajectory is well-approximated by the model, but once the two diverge, the estimated bounds are overly optimistic.

The iterative least-squares estimators performed in general at the level given by the Cramér-Rao lower bound on the variance of an estimate of the target location. Since the Cramér-Rao bound is achievable, the bound appears therefore to be a useful indicator of the level of performance that one can obtain in bearings-only tracking with an appropriate model of the target's motion. The estimators can be designed to account for *a priori* information on the target state, when that information can be expressed as a Gaussian distribution. Some preliminary results from an iterative least-squares estimator based on a constant speed target model show that the estimation algorithm becomes sensitive to the initial guess and frequently finds false, local minima. Additional research should be done to determine the feasibility of adding additional degrees of freedom to the model of target motion to reduce the degree of possible mismatch between the model and the actual motion of the target, particularly for long observation times, and also to find methods for incorporating *a priori* information on the target state in a form that reflects more accurately the likely behavior of the targets of interest but that does not cause the estimator algorithm to halt at false minima.

6. CONCLUSIONS

From the formulae for the Fisher information matrix, Equation (2.12), and for the Cramér-Rao bound, Equation (2.13), it is possible to determine how the bound depends on the angular accuracy of the measurements, on the rate at which samples are taken, and on the maneuvers performed by the sensor platform. In the absence of *a priori* information, the bound is proportional to the variance of the bearing measurements and to the measurement interval. Once *a priori* information is included, the dependence of the Cramér-Rao bound on these measurement parameters becomes more complicated, but when enough data are collected to give a more accurate estimate than the *a priori* information affords, the *a priori* information no longer has much effect on the bound.

An approximation to the Cramér-Rao bound was computed for a two-parameter family of sensor maneuver trajectories and plotted as contours vs the two parameters. The plots disclosed the existence of multiple local minima in the bound and of one, or sometimes two global minima. The optimal maneuver cycle time appears to be approximately a fixed fraction of the total observation time allotted to the target state measurement. The bounds were relatively insensitive to whether the target was crossing or moving radially, or to whether it was moving along a parabolic or a straight path, although it appears that the heading of a crossing target can be more accurately measured than the heading of an inbound target.

Even if one can calculate the optimal maneuver for the sensor given the location of the target, the sensor platform will generally be unable to follow that trajectory, because the optimal maneuver depends on the actual target state, which is unknown, or because of other trade-offs in the maneuvers taken by the sensor platform. The bounds showed little sensitivity to whether the sensor maneuver was optimized correctly, over a range of target states, and did not depend strongly on whether the maneuver was optimized for target position measurement or for target heading measurement. The bound does depend on the maneuver cycle time, or equivalently, on the observation time for which the sensor maneuver was optimized. For example, doubling the cycle time for the maneuver approximately doubles the time required for a good estimate of the target's state, but once the doubled observation time has elapsed, the resulting target state estimate is more accurate than it would have been for the original cycle time. Likewise, if the cycle time is halved, the first estimate is available sooner, but at the original observation time the halved cycle time maneuver produces a less accurate estimate.

Simulations of a practical target state estimator with a constant acceleration model of target motion disclosed that the Cramér-Rao bound can be achieved by an iterative least-squares maximum *a posteriori* probability (MAP) estimator, and that the Hessian matrix computed by the iterative least-squares algorithm is consistent with the theoretical Cramér-Rao bounds. Since there exist estimators that achieve the performance given by the Cramér-Rao bound, the Cramér-Rao bound appears to provide a good indication of the performance that one can expect in practice in other geometries. However, if the target's motion does not match the constant acceleration

model sufficiently closely, the estimates diverge from the correct values. Because of the limitations on the applicability of constant acceleration target models, it appears to be worthwhile to investigate models of target motion that both match actual targets more closely and lead to feasible estimators.

APPENDIX
ITERATIVE LEAST-SQUARES ESTIMATOR EQUATIONS

The iterative least-squares procedure employed for these calculations is a modified Newton-Raphson method, as described in Reference 24, pp. 187-190. The algorithm searches for a local minimum of the error

$$J(\hat{\mathbf{x}}^t) = \sum_{n=1}^{N} [\mathbf{r}_n - \mathbf{h}(\hat{\mathbf{x}}^t, t_n)]^T \, \mathbf{R}_n^{-1} \, [\mathbf{r}_n - \mathbf{h}(\hat{\mathbf{x}}^t, t_n)] \quad , \tag{A.1}$$

where $\mathbf{r}_n$ is the n^{th} vector of measurements taken at time t_n, $\mathbf{h}(\hat{\mathbf{x}},t)$ is the predicted measurement vector, and $\mathbf{R}_n$ is the measurement correlation matrix. If the global minimum of the error is found, the estimate of the target state is the maximum likelihood estimate, since the *a posteriori* probability of finding a given set of data $\mathbf{R}$ given the target state vector $\mathbf{x}^t$ can be written in terms of the error $J(\hat{\mathbf{x}}^t)$ as

$$p(\mathbf{R} \,|\, \mathbf{x}^t) = K \exp[- \frac{1}{2} J(\mathbf{x}^t)] \tag{A.2}$$

for some constant K that depends on neither the state vector nor the data.

The Newton-Raphson iterative least-squares algorithm finds a target state vector at which the error reaches a minimum by means of the recursion [Reference 24, p. 187, Equation (4.5.1)]

$$\hat{\mathbf{x}}^t[k+1] = \hat{\mathbf{x}}^t[k] - \left\{ \frac{\partial^2 J(\mathbf{x}^t)}{\partial \mathbf{x}^{t2}} \bigg|_{\mathbf{x}^t = \hat{\mathbf{x}}^t[k]} \right\}^{-1} \left\{ \frac{\partial J(\mathbf{x}^t)}{\partial \mathbf{x}^t} \bigg|_{\mathbf{x}^t = \hat{\mathbf{x}}^t[k]} \right\}^T \quad , \tag{A.3}$$

where

$$\frac{\partial J(\mathbf{x}^t)}{\partial \mathbf{x}^t} \bigg|_{\mathbf{x}^t = \hat{\mathbf{x}}^t[k]} \tag{A.4}$$

is the gradient $\nabla_{\mathbf{x}^t} J(\mathbf{x}^t)$ of the error with respect to the parameter vector, evaluated at the current estimate of the parameter vector, and where

$$\frac{\partial^2 J(\mathbf{x}^t)}{\partial \mathbf{x}^{t2}} \bigg|_{\mathbf{x}^t = \hat{\mathbf{x}}^t[k]} \tag{A.5}$$

is the Hessian of $J(\mathbf{x}^t)$, that is, the matrix of derivatives $\partial^2 J(\mathbf{x}^t)/\partial x_\mu^t \partial x_\nu^t$ with respect to each of the components x_μ^t of the state vector $\mathbf{x}^t$. The Newton-Raphson algorithm is modified by replacing the exact Hessian $\partial^2 J(\mathbf{x}^t)/\partial x_\mu^t \partial x_\nu^t$ by the expression (Reference 24, pp. 189-190)

$$J''_{\mu\nu}[k] = 2 \sum_{n=1}^{N} \left\{ \frac{\partial \mathbf{h}(\mathbf{x}^t, t_n)}{\partial x_\mu^t} \bigg|_{x^t = \hat{x}^t[k]} \right\}^T \mathbf{R}_n^{-1} \left\{ \frac{\partial \mathbf{h}(\mathbf{x}^t, t_n)}{\partial x_\nu^t} \bigg|_{\mathbf{x}^t = \hat{\mathbf{x}}^t[k]} \right\} \quad , \tag{A.6}$$

and by replacing the update equation by

$$\hat{\mathbf{x}}^t[k+1] = \hat{\mathbf{x}}^t[k] - \alpha_k[\mathbf{J}'']^{-1} \left\{ \left. \frac{\partial J(\mathbf{x}^t)}{\partial \mathbf{x}^t} \right|_{\mathbf{x}^t=\hat{\mathbf{x}}^t[k]} \right\}^T \quad , \tag{A.7}$$

where α is chosen to minimize the new error. In the implementation for this study, only $\alpha = 1, 1/2, 1/4, \ldots$ were tested, and the first value of α in this series that produced a new error smaller than the old error was selected. For the target state described in Equations (2.1) to (2.4), the approximation to the Hessian is given (Reference 8; Reference 24, pp. 187-190) by

$$\mathbf{J}''[k] = 2 \sum_{n=1}^{N} \mathbf{F}_n^T[k]\, \mathbf{H}_n^T[k]\, \mathbf{R}_n^{-1} \mathbf{H}_n[k]\, \mathbf{F}_n[k] \tag{A.8}$$

and the gradient by

$$\frac{\partial J(\mathbf{x}^t)}{\partial \mathbf{x}^t} = -2 \sum_{n=1}^{N} \mathbf{F}_n^T[k]\, \mathbf{H}_n^T[k]\, \mathbf{R}_n^{-1}[\mathbf{z}_n - \mathbf{h}(\mathbf{x}^t, t_n)] \quad , \tag{A.9}$$

where $\mathbf{H}_n[k]$ is the measurement gradient vector defined in Equation (2.8) at the time of the n^{th} measurement, and where $\mathbf{F}_n[k]$ is the propagator matrix from time t_n to the present time t_N, with the form shown in Equation (2.4), but with T_s replaced by $t_N - t_n$. Since the target and sensor were assumed to be coplanar, the derivatives with respect to the elevation angle ϕ are dropped from $\mathbf{H}_n[k]$ and the propagator matrix $\mathbf{F}_n[k]$ has just two blocks instead of three.

The *a posteriori* probability density of the target state assuming a zero-mean Gaussian *a priori* distribution of the target state is

$$p(\hat{\mathbf{x}}^t|\mathbf{R}) = K' \exp\left\{ -\frac{1}{2}\left[J + \frac{(\dot{x}^t)^2 + (\dot{y}^t)^2}{\sigma_v^2} + \frac{(\ddot{x}^t)^2 + (\ddot{y}^t)^2}{\sigma_a^2} \right] \right\} \quad , \tag{A.10}$$

K' being a normalization constant, and σ_v and σ_a the *a priori* standard deviations of the target's velocity and acceleration, respectively. The distributions of the velocity and the acceleration of the target were folded into the iterative least-squares algorithm by adding the terms

$$\frac{(\dot{x}^t)^2 + (\dot{y}^t)^2}{\sigma_v^2} + \frac{(\ddot{x}^t)^2 + (\ddot{y}^t)^2}{\sigma_a^2} \tag{A.11}$$

to the error and by making the necessary additions to the Hessian and to the gradient of the error with respect to the state vector. With these additional terms, the iterative least-squares estimate becomes a maximum *a posteriori* (MAP) estimator, since it finds the global minimum of

$$J_{MAP} = J + \frac{(\dot{x}^t)^2 + (\dot{y}^t)^2}{\sigma_v^2} + \frac{(\ddot{x}^t)^2 + (\ddot{y}^t)^2}{\sigma_a^2} \quad . \tag{A.12}$$

The approximation to the Hessian for J_{MAP} corresponding to Equation (A.6) is nearly identical in form to twice the Fisher information matrix for estimating $\mathbf{x}^t$ with prior information, with the exception that the present quantity is evaluated along the estimated target trajectory rather than along the actual trajectory.

ACKNOWLEDGMENT

The author would like to thank Dr. C.B. Chang for encouragement and for many fruitful technical discussions.

REFERENCES

1. S.C. Nardone and V.J. Aidala, "Observability Criteria for Bearings-Only Target Motion Analysis," IEEE Trans. Aerosp. Electron. Syst. **AES-17**, 162-166 (1981).

2. V.J. Aidala, "Kalman Filter Behavior in Bearings-Only Tracking Applications," IEEE Trans. Aerosp. Electron. Syst. **AES-15**, 29-39 (1979).

3. V.J. Aidala and S.E. Hammel, "Utilization of Modified Polar Coordinates for Bearings-Only Tracking," IEEE Trans. Automat. Contr. **AC-28**, 283-294 (1983).

4. S.E. Hammel, V.J. Aidala, K.F. Gong, and A.G. Lindgren, "Recursive versus Batch Processing Algorithms for Bearings-Only Tracking," *in Proceedings OCEANS '83, Effective Use of the Sea: An Update* (IEEE, New York, 1983), vol. 1, pp. 50-61.

5. R.M. Brown, "Emitter Location Using Bearing Measurements from a Moving Platform," Report No. 8483, Naval Research Laboratory (5 June 1981), DDC AD-A099808.

6. T.B. Ballard and R. Scott Hebbert, "A Tracking Algorithm Using Bearing Only," Report No. NSWC/WOL/TR-75-150, Naval Surface Weapons Center (20 October 1975), DDC AD-A045004.

7. A.C. Bamford, E.M.L. Beale, J. Lee, and S. Patel, "The Use of Reciprocal Polar Co-ordinates in Passive Tracking," Proc. 6th MIT/ONR Workshop on C^3 Systems, Cambridge, Massachusetts, 25-29 July 1983, pp. 198-201.

8. C.B. Chang, "Ballistic Trajectory Estimation with Angle-Only Measurements," IEEE Trans. Automat. Contr. **AC-25**, 474-480 (June 1980).

9. S. Fagerlund, "Target Tracking Based on Bearing Only Measurements," Report No. LIDS-R-1003, MIT Laboratory for Information and Decision Systems (June 1980), DDC AD-A100758.

10. A. Grindlay, "Bearing-Only Tracking Algorithms," Report No. 8421, Naval Research Laboratory (July 1980), DDC AD-A088093.

11. A.G. Lindgren and K.F. Gong, "Position and Velocity Estimation Via Bearing Observations," Report No. 5260, Naval Underwater Systems Center (15 June 1977), DDC AD-A043692.

12. D.J. Murphy, B. Ravo, and J. Davis, "Noisy Bearings-Only Target Motion Analysis," Report No. 117, Naval Underwater Weapons Research and Engineering Station (May 1970), DDC AD-870885L.

13. M.W. Ockeloen and Ir. G.A. Willemsen, "Target Motion Analysis (TMA) with an Extended Kalman-filter Using Bearing and Frequency Measurements," Report No. LEOK TR 1982-02, Laboratory for Electronic Developments for the Armed Forces, TNO, The Netherlands (May 1982).

14. E.J. Ohlmeyer, "Application of a Kalman Filter Passive Targeting Algorithm to Fleet Air Defense," Report No. 81-368, Naval Surface Weapons Center (November 1982), DDC AD-B095214L.

15. V. Petridis, "A Method for Bearings-Only Velocity and Position Estimation," IEEE Trans. Automat. Contr. **AC-26**, 488-493 (April 1981).

16. H. Weiss and J.B. Moore, "Improved Extended Kalman Filter Design for Passive Tracking," IEEE Trans. Automat. Contr. **AC-24**, 807-811 (August 1980).

17. W.W. Willman, "Modifications of a Ship Tracking Algorithm for Maneuver Following and Bearings-Only Data," Memorandum Report No. 4579, Naval Research Laboratory (1 October 1981), DDC AD-A104805.

18. W.W. Willman, "An Improved Procedure for Adaptive Estimation of Maneuvering in a Ship Tracking Algorithm," Memorandum Report No. 4813, Naval Research Laboratory (21 April 1982), DDC AD-A113351.

19. M.J. Hinich, "Passive Target Location Using Bearings from a Platform Whose Track Is Uncertain," IEEE Trans. Inf. Theory **IT-26**, 375-378 (May 1980).

20. G.J. Olsder, "On the Optimal Maneuvering During Bearings-Only Tracking," Proc. 23rd Conference on Decision and Control, Las Vegas, December 1984, pp. 935-940.

21. W.W. Willman, Naval Weapons Center, private communication.

22. H.L. Van Trees, *Detection, Estimation, and Modulation Theory: Part 1* (Wiley, New York, 1968).

23. J.H. Taylor, "The Cramér-Rao Estimation Error Lower Bound Computation for Deterministic Nonlinear Systems," IEEE Trans. Automat. Contr. **AC-24**, 343-344 (1979).

24. M.H.A. Davis and R.B. Vinter, *Stochastic Modeling and Control* (Chapman and Hall, London and New York, 1985).

REPORT DOCUMENTATION PAGE

1a. REPORT SECURITY CLASSIFICATION Unclassified	1b. RESTRICTIVE MARKINGS
2a. SECURITY CLASSIFICATION AUTHORITY	3. DISTRIBUTION/AVAILABILITY OF REPORT Approved for public release; distribution is unlimited.
2b. DECLASSIFICATION/DOWNGRADING SCHEDULE	
4. PERFORMING ORGANIZATION REPORT NUMBER(S) Technical Report 809	5. MONITORING ORGANIZATION REPORT NUMBER(S) ESD-TR-88-165
6a. NAME OF PERFORMING ORGANIZATION Lincoln Laboratory, MIT 6b. OFFICE SYMBOL *(If applicable)*	7a. NAME OF MONITORING ORGANIZATION Electronic Systems Division
6c. ADDRESS *(City, State, and Zip Code)* P.O. Box 73 Lexington, MA 02173-0073	7b. ADDRESS *(City, State, and Zip Code)* Hanscom AFB, MA 01731-5000
8a. NAME OF FUNDING/SPONSORING ORGANIZATION Naval Anti-Air Warfare (AAW) Technology 8b. OFFICE SYMBOL *(If applicable)*	9. PROCUREMENT INSTRUMENT IDENTIFICATION NUMBER F19628-85-C-0002
8c. ADDRESS *(City, State, and Zip Code)* Office of the Assistant Secretary of the Navy The Pentagon Washington, DC 20350	10. SOURCE OF FUNDING NUMBERS PROGRAM ELEMENT NO. 63103N 62712N; PROJECT NO. 401; TASK NO.; WORK UNIT ACCESSION NO.
11. TITLE *(Include Security Classification)* Tracking Targets with Bearing Data from a Single Sensor	
12. PERSONAL AUTHOR(S) William H. Gilson	
13a. TYPE OF REPORT Technical Report 13b. TIME COVERED FROM _____ TO _____	14. DATE OF REPORT *(Year, Month, Day)* 1989, January 13 15. PAGE COUNT 70
16. SUPPLEMENTARY NOTATION None	

17. COSATI CODES			18. SUBJECT TERMS *(Continue on reverse if necessary and identify by block number)*
FIELD	GROUP	SUB-GROUP	Cramér-Rao bounds; lower bounds; sensor-target geometry; iterative least squares; optimal angle-only tracking; extended Kalman filter

19. ABSTRACT *(Continue on reverse if necessary and identify by block number)*

This report examines performance limits (Cramér-Rao bounds) on tracking a maneuvering target using bearing measurements from a single sensor on a maneuvering platform. An approximation to the Cramér-Rao bound for estimating the location, velocity, and acceleration of a constant acceleration target with a prior distribution of the target's velocity and acceleration is derived for the case where the target and the sensor are coplanar. The bound is computed for members of a two-parameter family of sensor trajectories, and optimal sensor trajectories within this two-parameter family are identified from contour plots of the bound vs the two parameters. The optimal trajectory in most cases is a weave around the line of sight to the target, with a period which is proportional to the observation time allotted for the measurement. The bound on performance is not in general very sensitive to either the sensor's or the target's motion, or to mismatch between the two, except that the period of the sensor's weave pattern influences both the time at which good estimates become available and the variance of the estimates after a given time interval.

The bounds indicate that passive ranging techniques should achieve rms range accuracies on the order of 10 to 20 percent, after 40 s of maneuvering, when the target bearing is measured with a 0.3° standard deviation bearing at a 1-s update rate. Range rate accuracies are expected to be relatively poor. Simulations of an iterative least squares maximum *a posteriori* probability (MAP) estimator showed that the estimator performs at the level given by the bound and that it generates consistent estimates of the track accuracies. The estimator proved to be sensitive to target maneuvers that were not modeled within the estimation algorithm.

20. DISTRIBUTION/AVAILABILITY OF ABSTRACT ☐ UNCLASSIFIED/UNLIMITED ☒ SAME AS RPT. ☐ DTIC USERS	21. ABSTRACT SECURITY CLASSIFICATION Unclassified
22a. NAME OF RESPONSIBLE INDIVIDUAL Lt. Col. Hugh L. Southall, USAF	22b. TELEPHONE *(Include Area Code)* (617) 981-2330 22c. OFFICE SYMBOL ESD/TML